Resource

Cell

Mapping Synaptic Input Fields of Neurons with Super-Resolution Imaging

Graphical Abstract

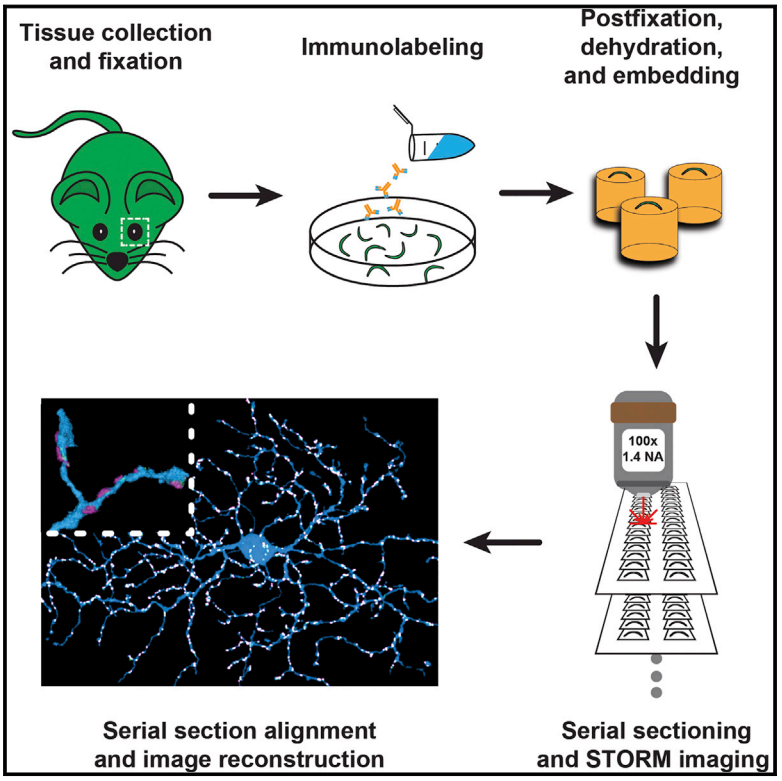

Authors

Yaron M. Sigal, Colenso M. Speer, Hazen P. Babcock, Xiaowei Zhuang

Correspondence

zhuang@chemistry.harvard.edu

In Brief

A super-resolution fluorescence-imaging platform for multi-color volumetric reconstruction of synapses and neurons in brain tissue is developed, enabling interrogation of neural circuitry at the nanoscale.

Highlights

- A super-resolution platform for volumetric tissue imaging and analysis is developed
- The platform allows synapses on neurons to be identified with molecular specificity
- On-Off DSGCs receive receptor subunit-specific GABAergic inputs
- On-Off DSGCs do not receive substantial monosynaptic glycinergic inputs

Sigal et al., 2015, Cell *163*, 493–505
October 8, 2015 ©2015 Elsevier Inc.
http://dx.doi.org/10.1016/j.cell.2015.08.033

CellPress

Resource

Cell

Mapping Synaptic Input Fields of Neurons with Super-Resolution Imaging

Yaron M. Sigal,[1,4] Colenso M. Speer,[1,4] Hazen P. Babcock,[2] and Xiaowei Zhuang[1,2,3,*]
[1]Howard Hughes Medical Institute, Department of Chemistry and Chemical Biology
[2]Center for Brain Science
[3]Department of Physics
Harvard University, Cambridge, MA 02138, USA
[4]Co-first author
*Correspondence: zhuang@chemistry.harvard.edu
http://dx.doi.org/10.1016/j.cell.2015.08.033

SUMMARY

As a basic functional unit in neural circuits, each neuron integrates input signals from hundreds to thousands of synapses. Knowledge of the synaptic input fields of individual neurons, including the identity, strength, and location of each synapse, is essential for understanding how neurons compute. Here, we developed a volumetric super-resolution reconstruction platform for large-volume imaging and automated segmentation of neurons and synapses with molecular identity information. We used this platform to map inhibitory synaptic input fields of On-Off direction-selective ganglion cells (On-Off DSGCs), which are important for computing visual motion direction in the mouse retina. The reconstructions of On-Off DSGCs showed a GABAergic, receptor subtype-specific input field for generating direction selective responses without significant glycinergic inputs for mediating monosynaptic cross-over inhibition. These results demonstrate unique capabilities of this super-resolution platform for interrogating neural circuitry.

INTRODUCTION

Mapping synaptic connectivity at multiple scales, ranging from the synaptic fields of individual neurons to the wiring diagram of the whole brain, is important for understanding how neural circuits function and how circuit defects contribute to mental illness (Alivisatos et al., 2013; Morgan and Lichtman, 2013). An ideal platform for imaging synaptic connectivity should provide (1) high-resolution structural information for reliable identification of synaptic connections and accurate assignment of synapses to neurons; (2) the ability to image specific molecules, such as neurotransmitter receptors, important for determining synapse identity and properties; and (3) automated image segmentation capability for efficient analysis of large-volume reconstructions that capture entire neurons or circuits.

Both fluorescence microscopy and electron microscopy (EM) have been used for volumetric neural circuit reconstruction (Helmstaedter, 2013; Kleinfeld et al., 2011; Lichtman and Denk, 2011). EM provides exquisite spatial resolution and membrane contrast for accurate synapse identification, and the high imaging speed of modern EM instruments allows increasingly larger volume reconstructions (Helmstaedter, 2013; Kleinfeld et al., 2011; Lichtman and Denk, 2011). However, because of the stringent fixation and sample preparation conditions required for high-quality EM imaging, labeling of endogenous synaptic proteins for determining the molecular identities and functional properties of synapses remains a difficult task for large-volume EM reconstructions. In addition, automated segmentation of EM images is still challenging and remains a bottleneck for scaling up neural circuit analysis, though substantial progress has been made on the development of automated EM image analysis and crowd-sourcing methods (Chklovskii et al., 2010; Helmstaedter, 2013; Jain et al., 2010). In comparison, fluorescence microscopy is compatible with immunohistochemistry and imaging of endogenous proteins over large volumes (Kleinfeld et al., 2011; Miyawaki, 2015), and multi-colored fluorescence signals can also help simplify the task of automated image segmentation for efficient data analysis. However, the diffraction-limited resolution of fluorescence microscopy can lead to substantial errors in the identification and assignment of synapses within reconstructed circuits.

Super-resolution fluorescence imaging overcomes the diffraction limit (Hell, 2007; Huang et al., 2010) and may enhance our ability to reconstruct neural circuits by integrating high image resolution for synapse identification and assignment, protein-specific labeling for determining the molecular properties of synapses, and multi-color imaging for efficient data analysis. Here, we developed a super-resolution reconstruction platform by combining stochastic optical reconstruction microscopy (STORM) (Huang et al., 2010; Rust et al., 2006) with serial ultrathin sectioning for large-volume reconstruction of endogenous molecular targets in tissues and used this platform to image entire neurons and their synaptic inputs. We focused our studies on the inner plexiform layer (IPL) of the mouse retina where diverse classes of retinal ganglion cells (RGCs) integrate synaptic inputs (Anderson et al., 2011; Helmstaedter et al., 2013) to generate unique spatiotemporal representations of the visual scene (Gollisch and Meister, 2010). A classic example of such a computation is the determination of visual stimulus motion direction by On-Off direction-selective RGCs (On-Off DSGCs) (Vaney et al., 2012). The substantial prior knowledge of the structure

and function of this cell type allows validation of our method, while unresolved structural questions in this system provide an opportunity to test the ability of our approach to extract novel biological information. For example, On-Off DSGCs are known to receive asymmetric inhibitory GABAergic inputs from presynaptic starburst amacrine cells (SACs) during null-direction stimulus movement (Briggman et al., 2011; Fried et al., 2002; Wei et al., 2011), and the α2 subunit of GABA(A) receptor plays an important role in this direction selectivity (Auferkorte et al., 2012). In addition to GABAergic synapses, glycinergic signaling also impacts the response of On-Off DSGCs to the edges of moving stimuli (Caldwell et al., 1978; Jensen, 1999), likely reflecting crossover inhibition between the on and off sublaminae mediated by glycinergic amacrine cells (Kittila and Massey, 1995; Stasheff and Masland, 2002; Werblin, 2010). However, the structural basis of this crossover inhibition in On-Off DSGC circuits is incompletely understood, and it is unclear whether glycinergic interneurons make direct synaptic contacts onto On-Off DSGCs. To demonstrate the capabilities of our super-resolution platform, we reconstructed the inhibitory synaptic input fields of individual On-Off DSGCs and determined the spatial distribution and neurotransmitter receptor identity of the synapses therein. We also reconstructed the inhibitory input fields of two other types of retinal neurons, a small-field On-center RGC and a narrow-field amacrine cell, for comparative demonstration.

RESULTS

Volumetric, Multi-color Super-Resolution Reconstruction

We labeled neurons and synaptic proteins with spectrally distinct photoswitchable dyes for multi-color STORM imaging (Dempsey et al., 2011). For neuron labeling, we used mice expressing GFP or YFP in the cytoplasm of a sparse subset of retinal neurons (Feng et al., 2000) and labeled the dissected retinal tissue with anti-GFP antibodies. For marking inhibitory synapses, we used an antibody against an inhibitory synapse scaffolding protein, gephyrin, which anchors glycine and/or GABA receptors at postsynaptic terminals (Tyagarajan and Fritschy, 2014). For presynaptic counter-staining, we used a cocktail of antibodies against several active zone proteins, bassoon, piccolo, munc13-1, and ELKS, for dense labeling of all presynaptic terminals. Table S1 shows all of the antibodies tested in this work. We also included a general neuropil stain, wheat germ agglutinin (WGA), in a fourth color channel to produce images with dense information content to assist serial-section alignment.

For volumetric reconstruction, we embedded tissues in resin and used serial ultrathin sectioning, in combination with STORM imaging, to generate large-volume super-resolution images. Serial ultrathin sectioning not only facilitates large-volume fluorescence reconstruction of tissue samples but also allows the image resolution along the z direction (as defined by the section thickness) to be substantially higher than the diffraction limit, as has been demonstrated previously in array tomography and three-dimensional (3D) STED reconstructions (Micheva and Smith, 2007; Punge et al., 2008). The partial exposure of epitopes in samples embedded in acrylic resin also allows many different synaptic proteins to be imaged through multiple rounds of post-embedding immunolabeling, which help identify synapses and characterize their molecular properties (Micheva et al., 2010; Micheva and Smith, 2007). However, the requirement of sample embedding for high-quality serial sectioning poses extra challenges for super-resolution imaging. Since STORM imaging relies on switching and localization of individual fluorophores to reconstruct super-resolution images (Huang et al., 2010; Rust et al., 2006), the resolution of a STORM image depends not only on the localization precision of individual fluorophores determined by their photon output but also on the localization density determined by the labeling density. Achieving optimal STORM resolution thus requires the labeling and embedding conditions to simultaneously retain optimal fluorophore properties and high-density labeling in resin-embedded samples. Resin embedding, however, substantially reduces the antigenicity of samples, which leads to a drastic reduction in antibody labeling density and severely compromises the image resolution achievable by STORM as we observed for tissues immunolabeled after acrylic resin embedding. Such low label densities, which are also evident in previous STORM images of tissue samples prepared using a similar post-embedding labeling approach (Nanguneri et al., 2012), prevent accurate tracing of neurons and identification of synapses using super-resolution imaging. We therefore explored pre-embedding immunofluorescence labeling (Punge et al., 2008) to increase the labeling density. We further tested various embedding materials and found that epoxy resin was excellent for maintaining the photon output of the fluorescent dyes. Finally, since optimal photoswitching of dye molecules requires access to a switching agent, such as thiol, we chemically etched the resin-embedded tissue sections using sodium ethoxide solution to expose the dyes to the thiol-containing imaging buffer.

Experimentally, we immunolabeled retinal tissues, performed an additional fixation step to crosslink the antibodies, dehydrated the samples, and embedded them in UltraBed epoxy resin (Figure 1A). The resin-embedded tissues were cut into 70 nm ultrathin sections, arrayed onto glass coverslips, and etched with sodium ethoxide (Figure 1A). Coverslips were imaged using a microscope setup that allowed automated imaging of entire arrays of sections, and both STORM and conventional images were collected for the same tissue sections. The xy-resolution of the STORM images was ~20 nm, and that of the conventional images was diffraction limited to ~200–300 nm, whereas the z resolution of both STORM and conventional images in this work was limited by the section thickness of 70 nm.

We developed an automated image analysis pipeline for processing STORM and conventional images, which included corrections of chromatic aberration and lens distortions using bead fiducials, as well as montage and serial-section alignment using scale-invariant feature transformation (SIFT) followed by elastic registration (Saalfeld et al., 2012) to generate large-volume reconstructions (Figure 1A) (see the Experimental Procedures for details). Volumetric STORM reconstructions of the IPL revealed efficient labeling throughout the sample, with neurons situated amidst hundreds of thousands of fluorescent clusters in each synaptic channel (Figures 1B, 1C, S1, and S2).

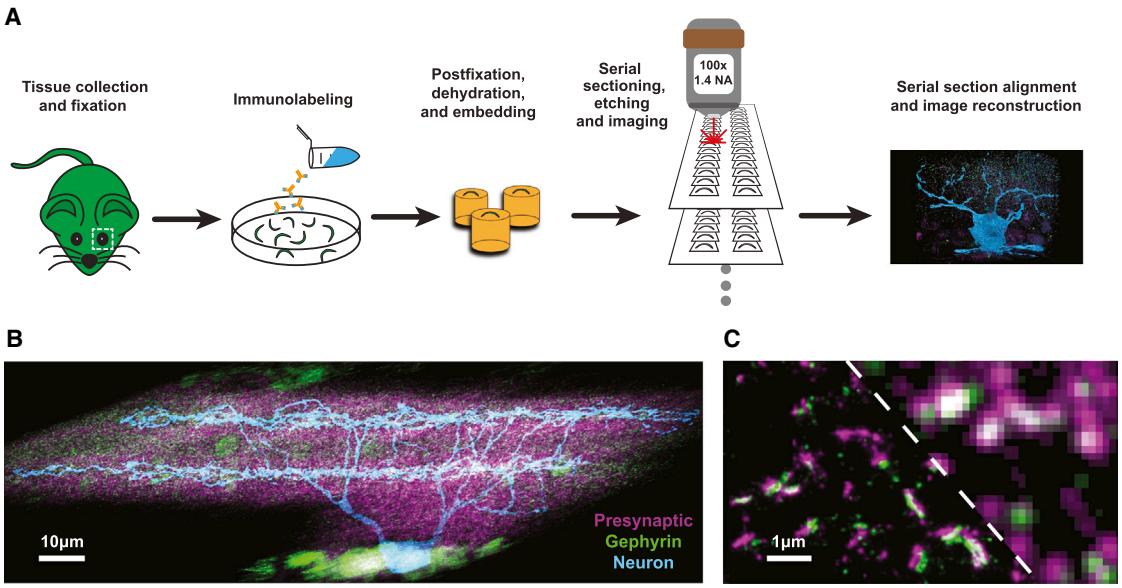

Figure 1. A Super-Resolution Imaging and Analysis Platform

(A) Tissues were dissected, fixed for immunohistochemical labeling, postfixed, dehydrated, and embedded in epoxy resin. Ultrathin sections were cut, arrayed on glass coverslips, and etched to expose fluorophores for STORM imaging. Individual serial sections were imaged and aligned to generate 3D reconstructions.

(B) STORM maximum intensity projection of a volume (2.3×10^5 µm^3) of the mouse IPL containing an On-Off DSGC (blue) amidst presynaptic (magenta) and gephyrin (green) clusters imaged using the platform.

(C) An enlarged image of synapses in a small region (1 µm thickness) of the IPL. For comparison, the corresponding conventional image of the upper right portion (to the right of the dashed line) is presented.

See also Figures S1 and S2.

Synapse Identification

Taking advantage of the multi-color super-resolution fluorescent signals, we developed image segmentation algorithms for automated neuron and synapse identification and performed quantitative analysis of entire fields of molecularly identified synapses in our datasets. Labeled synaptic proteins appear as clusters of localizations in STORM images, but not all clusters in STORM images represent synapses (Dani et al., 2010; Specht et al., 2013). For synapse identification, we measured the volume and signal density of all fluorescent clusters. In both presynaptic and postsynaptic (gephyrin) channels, these two parameters separated fluorescent clusters into two distinct populations (Figure 2A). We assigned the population of clusters with larger volumes as putative "synaptic" (S) structures and the other population with smaller volumes as putative "non-synaptic" (NS) structures. The vast majority (~91%) of the putative synaptic gephyrin clusters had closely apposed presynaptic clusters (Figures S3A and S3C), and example pairs of gephyrin and presynaptic clusters from this population clearly resembled synapses (Figure 2B), supporting our assignment. Of the putative non-synaptic population of gephyrin clusters, only a small fraction had a nearby presynaptic cluster (Figure S3A). Moreover, because some of these small gephyrin clusters were spatially close to the larger, paired gephyrin/presynaptic clusters and were thereby falsely identified as being paired, the automated pairing analysis of these small gephyrin clusters (Figure S3A) was less accurate than that for the larger synaptic clusters. Visual inspection showed that ~90% of these small gephyrin clusters were unpaired and likely represent gephyrin-containing trafficking vesicles or background signals from non-specific antibody labeling, whereas the remaining small fraction of paired structures could represent small (potentially immature) synapses.

For the presynaptic clusters, even the synaptic population contained a substantial fraction of clusters (~70%) that were not paired with gephyrin clusters (Figures S3B and S3D). This is expected, as the cocktail of antibodies against presynaptic active-zone proteins should label the presynaptic terminals of both excitatory and inhibitory synapses, and excitatory presynaptic terminals would not be expected to pair with gephyrin. The population of small presynaptic clusters did not show any appreciable pairing with gephyrin clusters (Figure S3B).

These analyses demonstrated that we could identify synapses based on the size and signal density of the fluorescent clusters observed in STORM images. In the following experiments, we focus our analysis on the population of synaptic clusters with larger volumes. In contrast, similar analysis of either gephyrin or presynaptic clusters observed in the corresponding conventional images did not allow clear distinction between synaptic and non-synaptic clusters (Figure S4A).

Examination of the hundreds of thousands of automatically identified synapses in STORM images of the inner retina showed non-uniform distributions across the depth of the IPL (Figure 2C). The difference between gephyrin-paired (inhibitory) and unpaired (putative excitatory) presynaptic cluster intensities divided the IPL into several sublaminae, two of which coincided with On-Off DSGC stratification in sublaminae S3

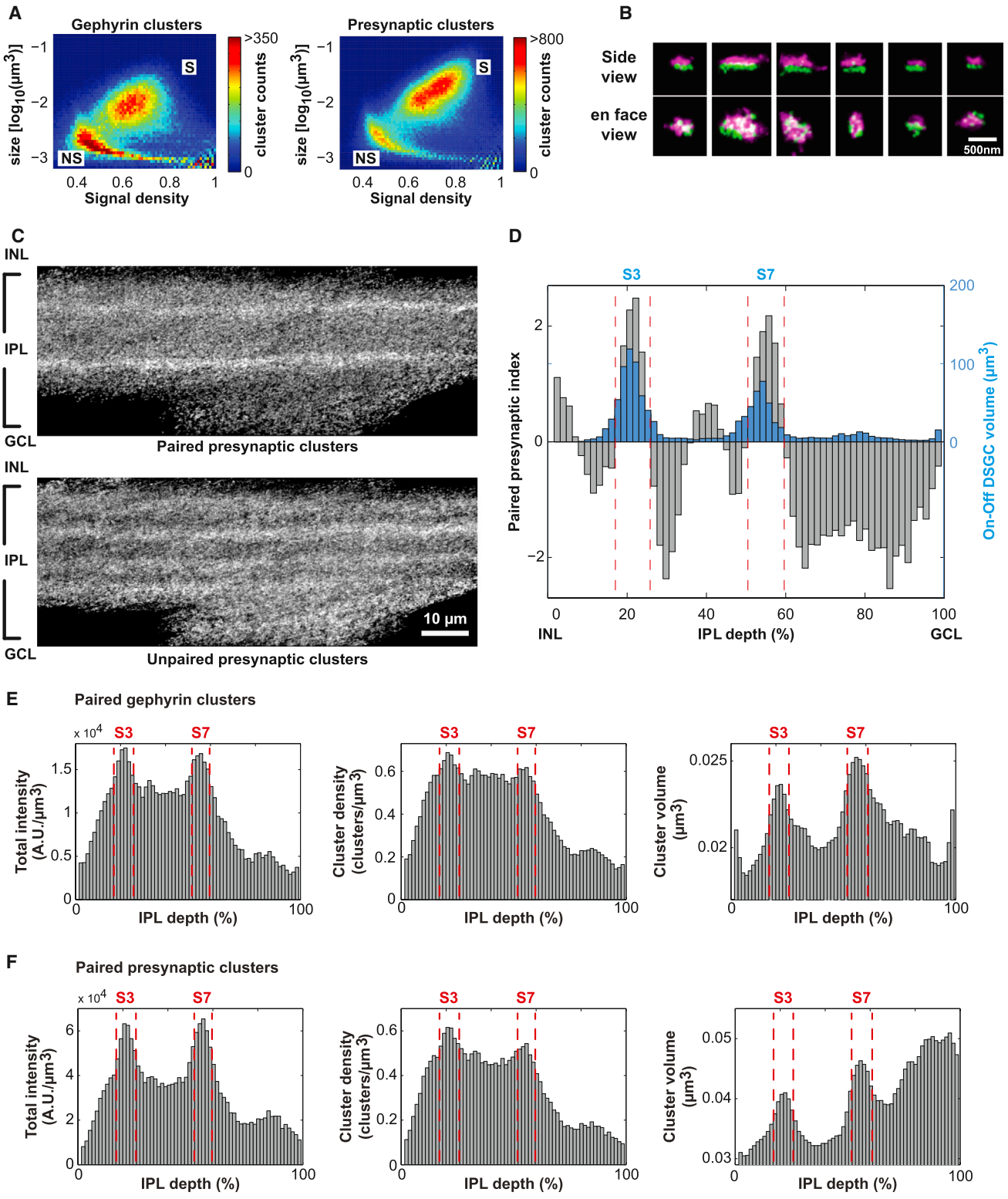

Figure 2. Automated Inhibitory Synapse Identification within the IPL

(A) Gephyrin (left) and presynaptic (right) clusters across the IPL can be separated into putative synaptic (S) and non-synaptic (NS) populations based on the volumes and signal densities of the clusters. Shown are the 2D distributions of cluster volume and signal density constructed from all gephyrin and presynaptic

(legend continued on next page)

and S7 (Figure 2D) (Vaney et al., 2012). Interestingly, the gephyrin and presynaptic signal intensities and the density and volumes of these gephyrin-positive inhibitory synapses all peaked in S3 and S7 (Figures 2E and 2F). As the size of inhibitory synapses correlates with synaptic strength (Lim et al., 1999; Nusser et al., 1997, 1998), this observation suggests that the inhibitory synapses subserving On-Off direction-selectivity may be among the strongest inhibitory connections in the mouse retina.

Identifying Inhibitory Synaptic Inputs to Labeled Neurons

To demonstrate the ability of our super-resolution platform to segment and analyze synaptic inputs onto identified neurons, we reconstructed two types of retinal ganglion cells and their associated inhibitory synaptic fields. Each of these datasets consisted of both STORM images (Figure 3A, left) and, for comparison, the corresponding conventional images (Figure 3A, right). To identify synaptic inputs onto neurons, we measured the density of gephyrin clusters and associated presynaptic signals as a function of distance to the neuron surface. Both density functions derived from STORM images were sharply peaked near the neuron surface with the gephyrin peak slightly inside the neuron and the presynaptic signal slightly outside the neuron as expected for input synapses (Figure 3B). These density peaks, in particular the gephyrin peak, were followed by a depletion zone, where the density dropped below the mean density of the surrounding IPL. For automated assignment of synapses to the neuron, we set a cutoff at the point where the gephyrin density dropped below the mean density of the surrounding IPL and selected only those gephyrin clusters located at a distance below the cutoff as synaptic inputs to the neuron (Figures 3B and 3D, left, and Movie S1).

Figure 3E and Movie S2 show the 1,017 inhibitory synapses assigned to a reconstructed On-Off DSGC. The number of synapses that we identified by STORM reconstruction here was similar to that estimated by previous EM reconstructions of SAC inputs to On-Off DSGCs (Briggman et al., 2011). Moreover, more than 98% of the synaptic gephyrin clusters assigned to the neuron had an apposing presynaptic partner. All of the gephyrin-presynaptic pairs assigned to the neuron were spatially oriented with the presynaptic structure more distant from the neuron than the postsynaptic structure (Figure 3C), which is consistent with these structures being input synapses onto the neuron. Together, these results further demonstrated the high accuracy in our synapse identification and assignment.

In comparison, assignment of synapses to neurons based on the corresponding conventional fluorescence images was less precise as the diffraction-limited resolution made it difficult both to identify synaptic clusters and also to set a proper cutoff value for assigning clusters to the neuron (Figure S4). As a result, this analysis resulted in substantial error rates (up to ~50%), depending on the selected cutoff distance (Figures 3D and S4C).

Distribution of Inhibitory Inputs to On-Off DSGCs

We next evaluated the size and position of all gephyrin-positive synapses within the dendritic arbor of each reconstructed cell. On-Off DSGCs, such as those shown in Figure 4A, exhibited non-random synapse distributions on both local and whole-cell scales (Figures 4B–4E). A Ripley's clustering analysis showed that synapses were significantly more depleted within ~1 μm of another synapse than would be predicted by a random distribution on the dendritic arbor (Figures 4B and S5A), likely reflecting a minimum inter-synapse spacing imposed by the finite size of each synapse, which is consistent with a previous observation (Bleckert et al., 2013). On the whole-cell scale, On-Off DSGCs exhibited sublaminar specificity with substantially higher synapse density in sublaminae S3 and S7 than in other sublaminae, even after normalization for the different surface areas of dendrites across the IPL depth (Figures 4C and S5B). This pattern is consistent with the specific innervation of On-Off DSGCs by SACs (Vaney et al., 2012), which also stratify in S3 and S7.

Distribution of Inhibitory Inputs to a Small-Field On-Center RGC

For comparison, we examined the sizes and spatial distribution of inhibitory synapses (936 total) onto a small-field On-center RGC (Figures 4F and 4G–4J and Movie S3), a putative type G6 as previously classified (Völgyi et al., 2009). Similar to On-Off DSGCs, synapses on this cell also exhibited a non-random spatial distribution on the local scale where Ripley's clustering analysis showed an ~1–2 μm depletion zone in the vicinity of each synapse (Figure 4G). However, the inhibitory synaptic input field of this neuron exhibited less sublaminar specificity than On-Off DSGCs on a whole-cell scale (Figure 4H).

Receptor Identity of Inhibitory Inputs to On-Off DSGCs

To demonstrate the capability of this super-resolution fluorescence reconstruction platform to determine the molecular identities of synaptic connections within neural circuits, we performed experiments to disambiguate different inhibitory synaptic input classes (GABAergic versus glycinergic) onto identified

clusters identified in the image block, with the cluster volume plotted on the log scale. The signal density is defined as the fraction of the volume occupied by the cluster that is positive for the gephyrin or presynaptic signal.

(B) Six example pairs of gephyrin (green) and presynaptic (magenta) clusters. The synapses are rotated to show side and en face views.

(C) Projection images of the IPL showing gephyrin-paired and unpaired synaptic clusters in the presynaptic channel. GCL: ganglion cell layer; INL, inner nuclear layer.

(D) The laminar distributions of the gephyrin-paired and unpaired presynaptic clusters divide the IPL into several sublaminae. Gray bars: presynaptic pairing index as a function of IPL depth. "Presynaptic pairing index" is calculated as the difference of the paired and unpaired presynaptic laminar intensity distributions after first standardizing each distribution to have a mean of zero and a SD of one. Blue bars: volume of the On-Off DSGC (μm^3) per 0.5 μm bin as a function of IPL depth.

(E) The total signal intensity (left), average cluster density (middle), and average cluster volume (right) for each cubic micron of imaged tissue measured as a function of depth within the IPL for gephyrin clusters that are paired with presynaptic clusters.

(F) Similar to (E) but for presynaptic clusters that are paired with gephyrin clusters.

The delineation of sublaminae S3 and S7 in (E) and (F) was determined based on (D). See also Figure S3.

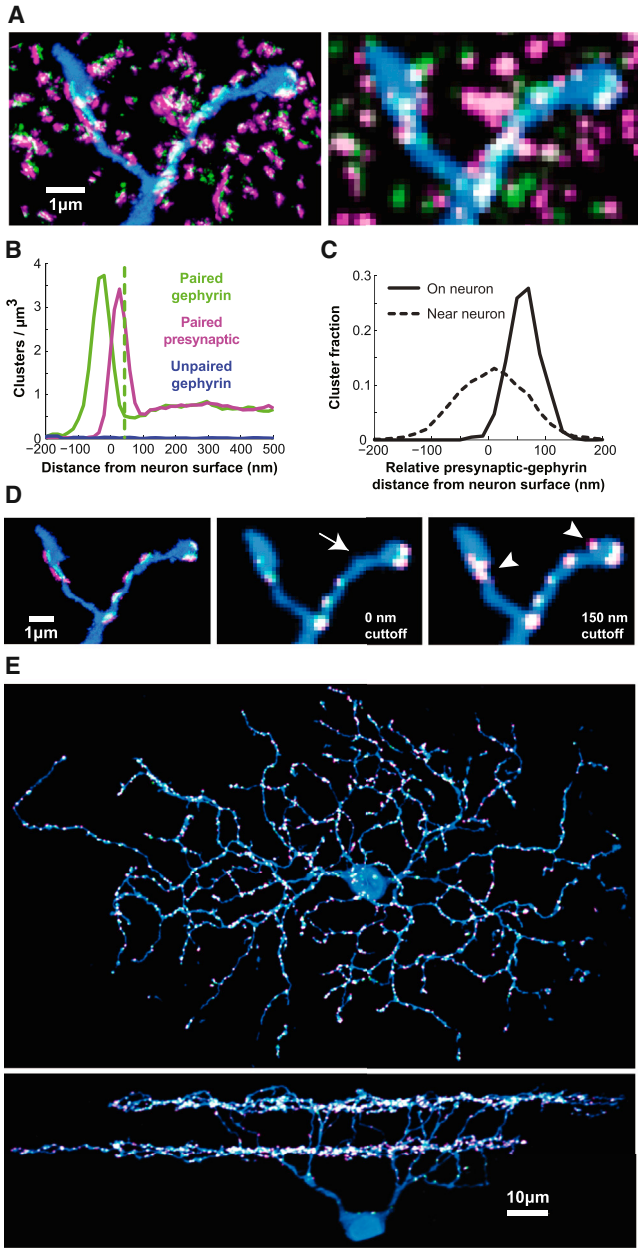

Figure 3. Automated Segmentation of Synaptic Inputs to Neurons

(A) STORM maximum projection image of a region containing a dendritic branch of a reconstructed On-Off DSGC (left) and the corresponding conventional image (right). Neurite is in blue, gephyrin in green, and presynaptic channel in magenta.

(B) The densities of the gephyrin clusters that are paired with presynaptic clusters (green trace), the unpaired gephyrin clusters (blue trace), and the gephyrin-paired presynaptic signal (magenta trace) measured as a function of the distance to the neuron surface. The distance at which the density peak of gephyrin clusters drops below the mean synapse density of the surrounding IPL (dashed green line) is used as a cutoff for defining gephyrin clusters on the neuron.

(C) For each synapse, we measured the distances of the presynaptic and postsynaptic signal to the neuron surface and defined the difference between these two distances as the relative presynaptic-gephyrin distance from the neuron surface. All synapses assigned to the On-Off DSGC show positive relative distance values (solid line), which is consistent with these pairs being input synapses onto the neuron. In contrast, the spatial arrangement of nearby synapses within 500 nm of the neuron (dashed line) shows a broad distribution of both positive and negative relative distance values, indicating a random orientation of nearby synapses with respect to the neuron surface.

(D) Assignment of synapses in the STORM image based on the cutoff selected in (B) reveals adjacent presynaptic and postsynaptic structures associated with the neuron (left). In contrast, assignment of synapses in the conventional images with a cutoff at 0 nm (middle) or 150 nm (right) show false-negative (arrows) and false-positive synapse assignments (arrowheads).

(E) En face view (top) and side view (bottom) of the STORM maximum intensity projection of a reconstructed On-Off DSGC (blue) with associated synaptic gephyrin (green) and presynaptic (magenta) clusters. Although gephyrin and presynaptic clusters are clearly resolved in the original reconstruction (Figure 3D and Movie S1), they appear as overlapping white dots here due to image downsampling.

See also Figure S4 and Movies S1 and S2.

neurons. We labeled retinae with either an antibody against the α2 subunit of the GABA(A) receptor (GABA(A)Rα2) or an antibody cocktail against all alpha subunits of glycine receptors (GlyRα1–4), in addition to antibodies against GFP and gephyrin for marking neurons and inhibitory synapses, respectively. To determine whether each gephyrin-positive inhibitory synapse contained GABA(A)Rα2 or glycine receptors, we examined whether the corresponding synaptic gephyrin cluster was paired with a specific receptor cluster by using the same approach described above for pairing presynaptic and postsynaptic structures (Figures S6A and S6B).

In GABA(A)Rα2-labeled samples, On-Off DSGC dendrites contained many GABA(A)Rα2-paired gephyrin clusters but strikingly rare unpaired gephyrin clusters (Figures 5A, 5B, and S6C). The gephyrin and GABA(A)Rα2 signal intensities in these synapses were strongly correlated with a Pearson coefficient of 0.82 (Figure S6E), suggesting that gephyrin intensity in these synapses correlates with synaptic strength, as is the case elsewhere in the nervous system (Lim et al., 1999; Nusser et al., 1997, 1998). Quantitatively, 97% ± 1% of the gephyrin-positive synapses on On-Off DSGCs contained GABA(A)Rα2, suggesting a high labeling efficiency of the receptors. Compared with synapses on On-Off DSGCs, only ~45% of all gephyrin-positive synapses analyzed across the IPL contained GABA(A)Rα2, demonstrating a strong enrichment of GABA(A)Rα2 in the synapses onto On-Off DSGCs. Although not all GABA receptor types are anchored at synapses by a gephyrin scaffold (Brickley and Mody, 2012; Tretter et al., 2012; Tyagarajan and Fritschy, 2014), gephyrin-independent GABA receptors are unlikely to contribute to direction selectivity (Brickley and Mody, 2012; Massey et al., 1997). This, together with the similar synapse counts observed between our experiments and previous EM reconstructions of SAC synapses onto On-Off DSGCs (Briggman et al., 2011), suggests that the vast majority, if not all, of the inhibitory synapses onto On-Off DSGCs are gephyrin positive. Hence, our observations suggest that nearly all of the inhibitory synapses onto On-Off DSGCs contain the GABA(A)Rα2 subunit.

In stark contrast to the GABA(A)Rα2-labeled samples, in the GlyRα1–4 labeled samples, we observed very few GlyRα1-4 positive synaptic gephyrin clusters on On-Off DSGCs (Figures 5C, 5D, and S6D). Quantitatively, only 8% ± 4% of the synaptic

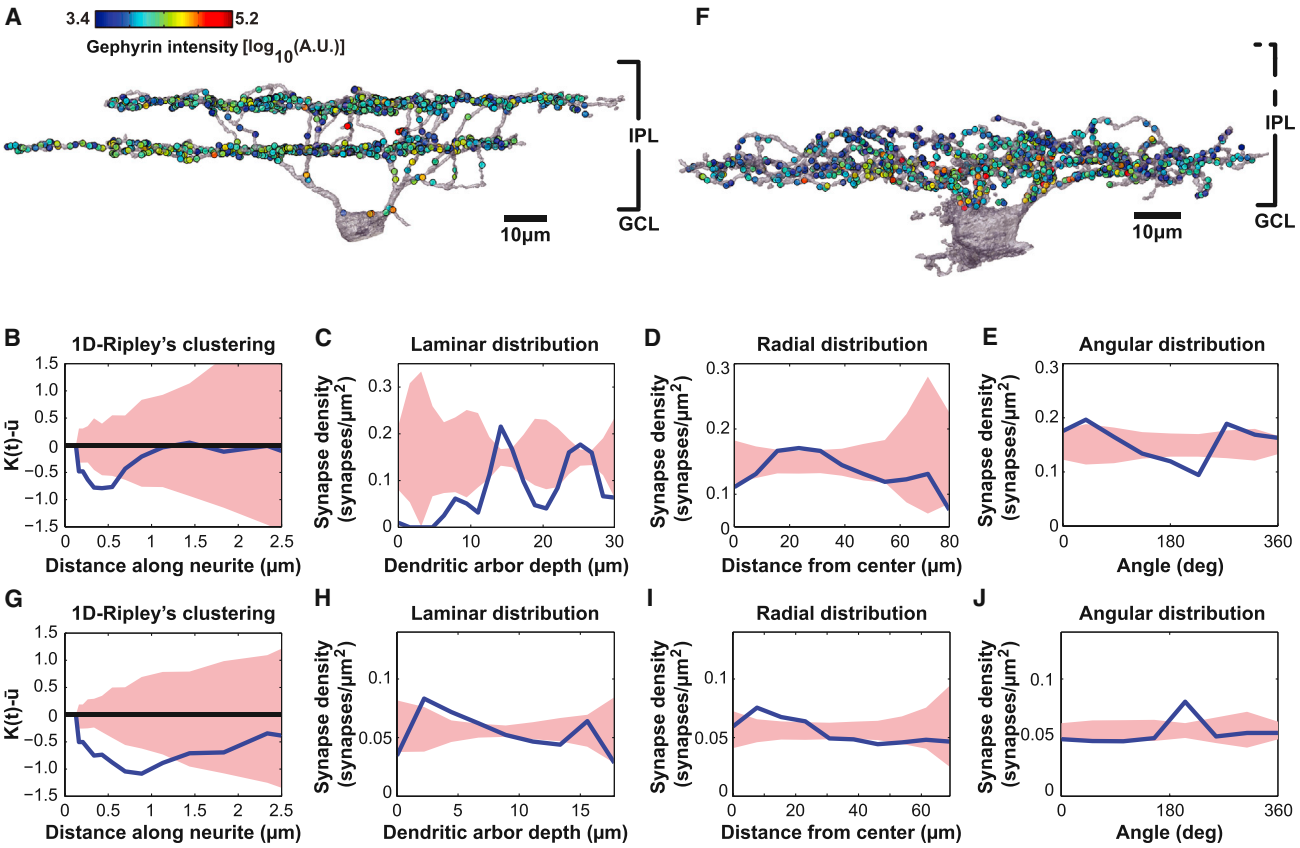

Figure 4. Distributions of Inhibitory Synapses on an On-Off DSGC and a Small-Field On-Center RGC

(A) Surface renderings of the On-Off DSGC (gray) shown in Figure 3E with all inhibitory synaptic inputs marked by circles whose color (blue to red) reflects gephyrin cluster intensity on a log scale.

(B) A one-dimensional Ripley's clustering analysis along the path of the skeletonized neuron. Negative value of the Ripley's function $K(t) - \overline{u}$ at short inter-synaptic distances indicate that, near any given synapse, the density of other synapses is significantly lower than a random distribution (see Experimental Procedures for the definition of Ripley's K function).

(C–E) The laminar (C), radial (D), and angular (E) distributions of the inhibitory synapse densities on the On-Off DSGC.

(F) Surface renderings of a small-field On-center RGC (gray) with all inhibitory synaptic inputs marked by circles whose color (blue to red) reflects gephyrin cluster intensity.

(G–J) Similar to (B–E) but for the On-center RGC.

Pink regions in (B–E) and (G–J) reflect 5/95% confidence intervals of random distributions derived from 1,000 randomizations of the synapse positions.

See also Figure S5 and Movies S2 and S3.

gephyrin clusters on On-Off DSGCs contained any GlyRα1-4 signal, and even these synapses exhibited extremely sparse GlyRα1–4 labeling relative to nearby glycine-positive synapses not on the labeled On-Off DSGCs (Figures S6F and S6G). Since these nearby synapses contained substantial GlyRα1–4 signal, the lack of GlyRα1–4 in the On-Off DSGC synapses could not be attributed to low receptor labeling efficiency. Moreover, while previous work has shown a strong correlation between glycine receptor and gephyrin expression at synapses (Specht et al., 2013), we observed little correlation between the intensity of gephyrin and GlyR signals for these GlyR-positive gephyrin clusters on the On-Off DSGCs (Figure S6E). These results suggest that these sparse, low-intensity GlyR punctae probably reflect non-specific background labeling, and even if they were specific synaptic labeling, they would contribute relatively little synaptic current due to the low receptor abundance. As gephyrin is required for clustering glycine receptors at synapses (Feng et al., 1998; Fischer et al., 2000; Kirsch et al., 1993), our results thus indicate that On-Off DSGCs in the mouse retina receive little monosynaptic glycinergic input.

In contrast to the STORM results, analysis of the corresponding conventional fluorescence images showed that a substantial population (20%–30%) of the gephyrin-labeled "synapses" assigned to On-Off DSGCs were GABA(A)Rα2 negative (Figure S7). These errors arise primarily from two sources: (1) it is difficult to separate synaptic gephyrin clusters from non-specific background labeling or trafficking vesicles containing gephyrin based on conventional images (Figure S4A), and hence some of the gephyrin clusters assigned to the neuron may not correspond to synapses; and (2) synapses near the neuron, but not on the neuron, can be mistakenly assigned to the neuron because of the limited resolution of the conventional images (Figure S4C).

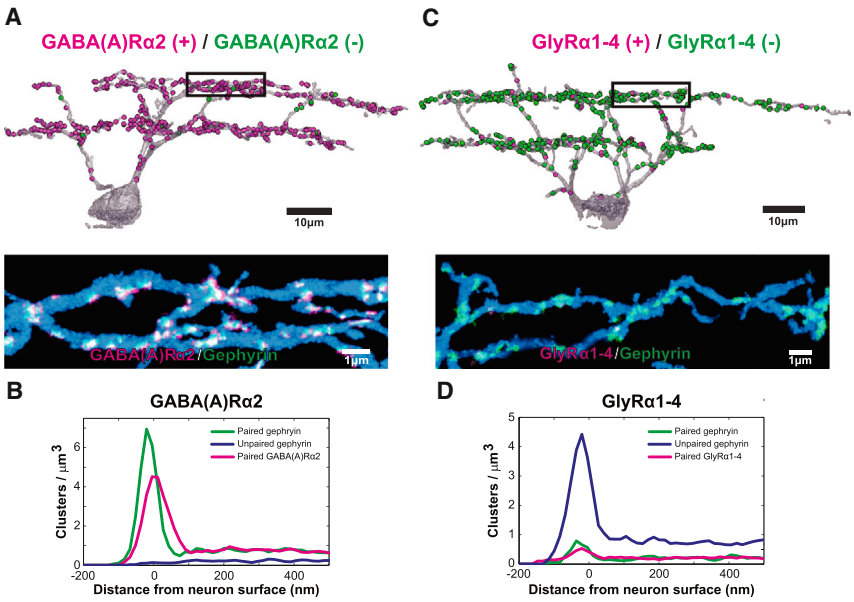

Figure 5. Receptor Identity of the Inhibitory Synaptic Inputs to On-Off DSGCs

(A) Top: surface rendering of a central cross-section of an On-Off DSGC (gray) with GABA(A)Rα2-positive (+) and GABA(A)Rα2-negative (−) inhibitory synapses marked as magenta and green circles, respectively. STORM image of the boxed region is shown in the bottom panel. Neuron: blue. Gephyrin: green. GABA(A)Rα2: magenta.

(B) The GABA(A)Rα2-paired gephyrin (green), gephyrin-paired GABA(A)Rα2 (magenta), and unpaired gephyrin cluster (blue) densities as a function of the distance to the neuron shown in (A).

(C) Top: surface rendering of a central cross-section of an On-Off DSGC (gray) with GlyRα1–4-positive (+) and GlyRα1–4-negative (−) inhibitory synapses marked as magenta and green circles, respectively. STORM image of the boxed region is shown in the bottom panel. Neuron: blue. Gephyrin: green. GlyRα1–4: magenta.

(D) The GlyRα1–4-paired gephyrin (green), gephyrin-paired GlyRα1–4 (magenta), and unpaired gephyrin cluster (blue) densities as a function of the distance to the neuron shown in (C).

See also Figures S6 and S7.

Inhibitory Inputs and Outputs of a Glycinergic Interneuron

Last, we imaged gephyrin-positive inhibitory synapses associated with a subtype of narrow-field amacrine cell (NFAC) (Figure 6A and Movie S4), putatively a Type 7 based on previous characterization (Pang et al., 2012). NFACs mediate crossover inhibition between On and Off sublaminae of the IPL via glycinergic inhibition (Werblin, 2010). In contrast to On-Off DSGCs, the surface of this NFAC was highly enriched with paired GlyRα1–4 and gephyrin clusters but largely depleted of unpaired, GlyRα1–4-negative gephyrin clusters (Figures 6A and 6B). The resolution of STORM allowed us to visualize the orientations of gephyrin-receptor pairs relative to the neuron surface and determine whether these structures were input synapses onto the cell or output synapses from the cell (Figure 6C). Unlike GABAergic synapses onto On-Off DSGCs, which were all input synapses (Figures 6D and 3C), the glycinergic synapses on the NFAC contain both input and output synapses (Figures 6C and 6D). Both synaptic inputs and outputs exhibited sublaminar specificity with enrichment in the Off sublaminae (Figure 6E), suggestive of this cell being an On-center responsive Type 7 glycinergic amacrine cell (Pang et al., 2012) providing crossover inhibitory output to the Off sublaminae (Werblin, 2010).

About 85% of the synapses on this neuron contained glycine receptors (Figure 6E), again indicating a high receptor labeling efficiency in our samples. Since NFACs are glycinergic cells, it is not surprising that the observed output synapses from this cell were mostly GlyRα1–4 positive. It is, however, interesting to observe that the majority of gephyrin-positive inputs onto this cell were also GlyRα1–4 positive, suggesting that this type of NFAC receives inhibitory input signals mainly from other glycinergic amacrine cells, though our results do not exclude the possibility that this cell type also receives some GABAergic inputs.

DISCUSSION

Mapping the spatial organization and molecular identity of synaptic connections within neuronal networks is important for understanding how the nervous system functions. Here, we developed a super-resolution platform for volumetric reconstruction and automated segmentation of endogenous molecular targets in tissue and demonstrated the ability of this platform to identify the spatial patterns and molecular identity of inhibitory synapses within neuropil, as well as onto individual neurons using the mouse retina as a model system.

This method provides several benefits for reconstructing synaptic connectivity. First, the superior resolution of this approach, as compared to conventional fluorescence imaging, allows more accurate identification of synapses and assignment of synapses to neurons. Indeed, when comparing results from the same tissue samples, we found that conventional fluorescence imaging led to substantial errors both in the identification of synapses and in the assignment of synapses to neurons even with the improved *z* resolution afforded by ultrathin sectioning. These errors resulted in misidentification of inhibitory synaptic types onto On-Off DSGCs, which could lead to substantial misinterpretation of cellular physiology. In addition, the resolution provided by STORM also allowed us to quantitatively measure synapse size, which is often a good indicator of synaptic strength (Nusser et al., 1997, 1998). This ability allowed us to map the relative strengths of inhibitory synapses at different locations both on identified neurons and across the IPL.

A second benefit of the super-resolution reconstruction platform is its ability to use standard immunohistochemistry for labeling multiple endogenous protein targets of interest, which allows the determination of the molecular identities of synapses. Such information is difficult to ascertain using EM reconstructions alone but is important for interpreting the function of specific synapses in neural circuits (Bargmann and Marder, 2013).

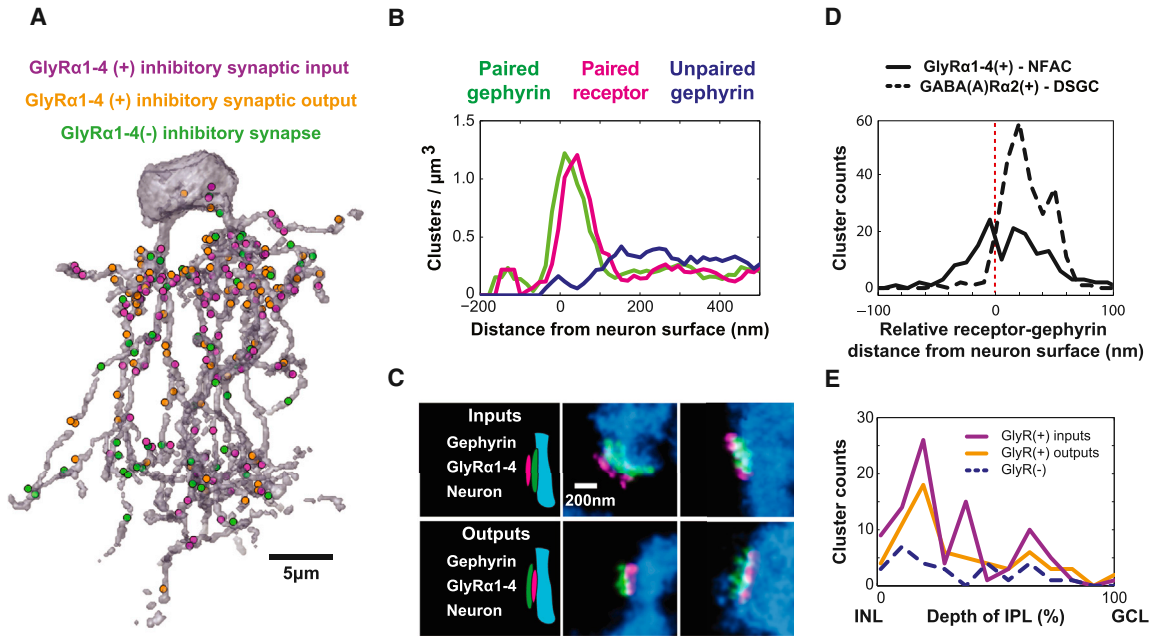

Figure 6. Input and Output Inhibitory Synapses of a NFAC

(A) Surface rendering of a NFAC (gray) with GlyRα1–4 (+) input (purple circles), output (orange circles), and GlyRα1–4 (−) synapses (green circles) shown.

(B) The GlyRα1–4-paired gephyrin (green), gephyrin-paired GlyRα1–4 (magenta), and unpaired gephyrin cluster (blue) densities as a function of the distance to the surface of the neuron.

(C) Examples of input and output synapses distinguished by the positions of receptor and gephyrin signals relative to the surface of the neuron. Input synapses have the gephyrin clusters (green) in the dendrites (blue) and receptor clusters (magenta) on the surface. Output synapses have the receptor cluster immediately adjacent to the dendrite surface and the gephyrin clusters farther outside.

(D) The relative displacement of receptor and gephyrin clusters from the neuron surface, with positive values indicating receptor being farther from the neuron (input synapses) and negative value indicating gephyrin being farther from the neuron (output synapses). The solid line shows the distribution for glycinergic synapses associated with the NFAC, and the dashed line shows the distribution for the GABAergic synapses associated with an On-Off DSGC.

(E) Laminar distributions of the input (purple) and output (orange) GlyRα1–4-positive synapses and the GlyRα1–4-negative synapses (blue) on the NFAC.

See also Movie S4.

Taking advantage of this capability, we showed that gephyrin-positive inhibitory synapses onto On-Off DSGCs were overwhelmingly GABAergic and each contained the GABA(A) receptor α2 subunit, suggesting that this receptor subunit is important for generating postsynaptic currents during motion detection. This result is consistent with previous data showing the enrichment of GABA(A)α2 in On-Off DSGC synapses and reduction in direction-selective responses in the GABA(A)α2 knockout mouse (Auferkorte et al., 2012). Our reconstructions also showed that On-Off DSGCs receive little, if any, monosynaptic glycinergic input. These structural data, together with the observations that blocking GABA receptors largely eliminates inhibitory currents in On-Off DSGCs (Stafford et al., 2014; Trenholm et al., 2011), suggest that glycinergic modulation of On-Off DSGCs does not occur via direct glycinergic inputs onto these neurons but likely through glycinergic inhibition of bipolar cells or SACs that are presynaptic to On-Off DSGCs (Ishii and Kaneda, 2014; Majumdar et al., 2009; Zhang and McCall, 2012).

A third strength of this reconstruction platform is its ability to perform automated segmentation of synaptic connections in neural circuits without manual annotation. This automated analysis capability greatly speeds up the image processing required to extract biological information from individual reconstructions. For example, the image processing for volumetric reconstruction and segmentation of a whole On-Off-DSGC cell and associated synapses took <3 days of computation time without any need for manual segmentation or correction. In this work, the rate-limiting step of our reconstructions was the STORM image acquisition time, as imaging an entire On-Off-DSGC of 2.3 × 10^5 μm^3 in four color channels took ~3 weeks using a STORM setup equipped with an EMCCD camera. Our recent switch to a scientific CMOS (sCMOS) camera with a larger field of view and higher frame rate (Huang et al., 2013) shortened the imaging time of a comparable volume to ~3 days. We envision this automated imaging and segmentation pipeline to be beneficial for determining neural circuit properties in different genetic mutant and disease models or at different time points during development, where a large number of reconstructions are needed.

One potential limitation of this super-resolution fluorescence platform, as compared with EM approaches, is the density of neuronal processes that can be reconstructed within a volume. In this work, we reconstructed the spatial distributions and molecular identities of synapses onto individual neurons in Thy1-GFP/YFP transgenic mice, in which only sparse subsets of neurons are labeled. We expect that our approach can be extended to the reconstruction of multiple, synaptically coupled

neurons using recently developed high-density, high-antigenicity, genetic labeling approaches (Cai et al., 2013; Loulier et al., 2014; Viswanathan et al., 2015) or by microinjection of probes to directly label multiple neurons. Although the image resolution here was limited in the z direction by the 70 nm section thickness, we anticipate a substantial improvement in z resolution by using 3D STORM (Huang et al., 2008). In particular, using high-precision z-localization approaches (Jia et al., 2014; Shtengel et al., 2009; Xu et al., 2012), the optical resolution can reach ~10 nm in all three dimensions. However, this resolution is still lower than that achievable by EM, and the labeling density may impose an additional limitation on resolution. Together, these may limit the density of neurites that can be reconstructed, and it remains to be determined whether this STORM platform can be used for dense reconstruction of all neurons in a volume.

With its unique capabilities complementary to existing reconstruction methods, we expect that this volumetric super-resolution reconstruction platform will enable a variety of synaptic connectivity analyses that will substantially enhance our understanding of the structural basis of nervous system function. The ability to reconstruct and identify endogenous molecular targets in large tissue volumes should also benefit the studies of many other biological systems.

EXPERIMENTAL PROCEDURES

Animals

Animal work was performed in accordance with protocols approved by the Institutional Animal Care and Use Committee at Harvard University. Adult transgenic mice (Tg(Thy-1-EGFP)MJrs/J or YFP (Tg(Thy1-YFP)HJrs/J, The Jackson Laboratory) (Feng et al., 2000), both male and female animals 6–24 weeks of age, were used in our experiments.

Retinal Tissue Preparation

Whole eye-cups were immersion fixed in 4% paraformaldehyde for 10–60 min at room temperature. Both whole-mount and vibratome-sectioned retinae were used for labeling. For whole-mount labeling, retinae were laid flat on nitrocellulose membranes, and individual labeled neurons were excised in circular punches (diameter ~500 μm, thickness ~200 μm). For vibratome section labeling, retinae were immersed in 37°C 2%–3% agarose, cooled on ice, and sectioned at 50–150 μm thickness in 1× DPBS.

Immunohistochemistry

Retinae were blocked in 10% normal donkey serum in 1× DPBS with 0.3% Triton X-100 and 0.02%–0.05% sodium azide for 2–3 hr at room temperature and incubated in primary antibody solutions diluted in blocking buffer overnight for 3–4 nights at 4°C. A complete list of all primary antibodies tested in this work is provided in Table S1 with the antibodies selected for the STORM reconstructions highlighted. Following primary antibody incubation, retinae were washed 6 times for 20 min each in 2% normal donkey serum in 1× DPBS at room temperature and incubated in secondary antibodies (detailed in the Supplemental Experimental Procedures) overnight at 4°C for 1–2 nights to label the neuron with photoswitchable dye Atto 488 and two synaptic targets (gephyrin and presynaptic proteins or gephyrin and receptors) with photoswitchable dyes Alexa Fluor 647 and DyLight 750, respectively. The antibodies for labeling synaptic proteins were also conjugated to Alexa Fluor 405 to facilitate photoactivation of Alexa Fluor 647 and DyLight 750. Retinae were then washed 6 times for 20 min each in 1× DPBS at room temperature and incubated overnight in Cy3B-labeled WGA.

Postfixation, Dehydration, and Embedding in Epoxy Resin

Labeled retinae were postfixed for 2 hr in 3% paraformaldehyde and 0.1% glutaraldehyde diluted in 1× DPBS. Postfixed retinae were dehydrated in a graded series of ethanol washes (50%/70%/90%/100% two times) for 10–20 min each and then incubated in UltraBed Epoxy Resin (Electron Microscopy Sciences) solutions of increasing concentration for 2 hr each (75% ethanol/25% resin; 50% ethanol/50% resin; 25% ethanol/75% resin; 100% resin 2 times). Dehydrated resin blocks were then polymerized in UltraBed overnight for 16 hr at 70°C.

Ultrathin Sectioning

Ultrathin sections were cut at 70 nm on a Leica UC7 Ultramicrotome (Leica Microsystems) using an ultra Jumbo diamond knife (Diatome). The section thickness was verified in two independent ways, as described in the Supplemental Experimental Procedures. Sections were collected on glass coverslips coated with 0.5% gelatin/0.05% chromium potassium sulfate. Coverslips were dried at 60°C for 25 min.

Preparation of Coverslips for Imaging

Coverslips of tissue sections were immersed in 10% sodium ethoxide solution for 5–20 min to etch the embedding resin for optimal photoswitching of dyes. Fluorescent beads (mixture of 540/560 and 715/755 FluoSpheres from Life Technologies, detailed in the Supplemental Experimental Procedures) were spotted on the coverslips as fiducial markers. Coverslips were secured to glass slide flow channels, filled with STORM imaging buffer (10% glucose/17.5 μM glucose oxidase/708 nM catalase/10 mM MEA/10 mM NaCl/200 mM Tris), and sealed with epoxy.

Imaging Setup

Imaging was performed through Olympus UPlanSApo 100× 1.4 NA oil-immersion objectives mounted on Olympus IX71 inverted microscopes with back optics arranged for oblique incident angle illumination. The microscope contained a custom pentaband dichroic and pentanotch filter (Chroma Technology Corp) and laser lines at 488/561/647/750 nm (detailed in the Supplemental Experimental Procedures) for excitation of Atto 488, Cy3B, Alexa Fluor 647, and DyLight 750, respectively. A 405 nm laser was used for reactivation of dyes. Images were acquired on an Andor iXon3 897 or 897Ultra EMCCD camera through a QV2 quadview image splitter (Photometrics). Each camera pixel corresponded to ~158 nm in sample space, and the total imaging field size was ~40 μm × 40 μm. Axial focus during imaging was maintained in an automated manner as described previously (Dempsey et al., 2011).

Automated Image Acquisition

Tissue sections and fiducial bead fields were initially located using a 4× objective. Regions of interest (ROIs) were subsequently identified with a 100× objective. The stage position coordinates for each ROI were determined, and the position list for all ROIs on a coverslip was then used to generate a master file that controlled laser illumination, camera activation, stage movement, AOTF control, and shutter sequences for automated STORM and conventional imaging. Each imaging session began with imaging of low-density bead fields by first exciting the 540/560 beads at 488 nm and detecting in the Alexa Fluor 647, Cy3B, and Atto 488 channels and then exciting the 715/755 beads at 752 nm and detecting in the DyLight 750 and Alexa Fluor 647 channels. These low-density bead images were used for chromatic aberration correction across different color channels.

Next, each ROI was imaged at the conventional resolution in each of the four color channels (DyLight 750, Alexa Fluor 647, Cy3B, and Atto 488). Next, images of the high-density bead field were acquired in each of the four color channels for (1) flat-field correction to compensate for non-uniform illumination across the field of view and (2) lens distortion correction at image field edges.

STORM imaging of individual ROIs was next performed in four color channels. For each ROI, the DyLight 750 channel was imaged for ~4K–4.5K frames at 30 Hz, the Alexa Fluor 647 channel was imaged for 6K–7K frames at 60 Hz, and the Cy3B and Atto 488 channels were each imaged for ~10K frames at 60 Hz. To ensure that overlapping regions in each montage were not bleached, STORM movies were collected in two passes for each ROI, each consisting of half the total number of frames described above.

STORM Image Analysis

STORM movies were analyzed to determine the positions of individual molecules using a DAOSTORM algorithm (Babcock et al., 2012; Holden et al., 2011). Molecule lists were rendered as 2D images with 15.8 nm pixel size, which is close to both our ~20 nm STORM image resolution and 1/10 of the camera pixel size. For consistency of analysis, the conventional images were up-sampled to 15.8 nm/pixel. Chromatic aberrations were corrected using the transformation maps generated from the low-density bead field images, and lens-induced optical distortions were corrected using transformation maps generated from the high-density bead field images, as detailed in the Supplemental Experimental Procedures.

Alignment of Multiple Image Tiles within Individual Sections

Each STORM image was aligned to the corresponding conventional image using two-dimensional cross-correlation (Guizar-Sicairos et al., 2008). For mosaic imaging, Scale-Invariant Feature Transformation (SIFT) (Lowe, 2004) was used to find points of similarity between overlapping regions in adjacent image tiles in the WGA channel and generate a rigid alignment transformation that was applied to the conventional and STORM images to stitch overlapping image tiles. On average, the residual offset in alignment between SIFT points of similarity in two adjacent image tiles was <40 nm.

Alignment of Serial Sections

Corresponding SIFT features between adjacent sections were used to determine a rigid linear transformation between sections, which was applied to all sections in the dataset to achieve a coarse, 3D rigid alignment of the data. Then, we applied elastic registration (Saalfeld et al., 2012) to further improve the alignment accuracy between adjacent sections while minimizing the global deformation of the entire image block. The warping transforms generated in these steps were applied to all conventional fluorescence and STORM channels.

Segmentation of STORM and Conventional Fluorescence Images

STORM images were first filtered using a mask generated from the conventional images to remove background and signals from occasional debris on the coverslip. To generate this mask, the signals in the conventional images were thresholded using the lower threshold of a two-level Otsu threshold method (Otsu, 1979) that divided the signals in our images into three classes with the lowest-intensity class representing the background, the highest intensity class representing neuronal and synaptic features, and the middle class representing other low-intensity signals above background. To identify the surface of the neuron, we smoothed the neuron signal with a Gaussian kernel with σ = 47 nm and then binarized the neuron signal using the lower threshold of the two-level Otsu threshold method. To identify fluorescent clusters in the gephyrin, presynaptic or receptor channels in the STORM images, we applied a 79 nm Gaussian convolution to the signal in the XY plane and an isometric Gaussian convolution (~1 voxel) in Z and used the lower threshold of the two-level Otsu threshold method to binarize the image and identify connected components in three dimensions. Additional separation of over-connected clusters was performed using a watershed transformation. Processing of conventional images was performed similarly, except that we binarized the conventional images based on the higher threshold of a two-level Otsu threshold.

Two-Dimensional Analysis to Separate Different Populations of Gephyrin and Presynaptic Clusters

To determine whether a given cluster was synaptic, two parameters were considered for each cluster in the gephyrin and presynaptic channels: the volume of the cluster was calculated from the connected components within the segmented image. Second, the signal density was measured as the fraction of volume of the connected components that was occupied by signal-positive voxels in the raw data. For STORM images, plotting the distribution of these two parameters constructed from all clusters in the dataset as a 2D histogram showed two peaks. Separation of the two populations is described in the Supplemental Experimental Procedures.

Ripley's K Function

The Ripley's K function is calculated as $K(t) = \lambda^{-1}\sum_{i\neq j} I(d_{ij} < t)/n$, where t is the distance along neurites, λ is the average density of synapses on the neuron skeleton, I is the indicator function, d_{ij} is the distance between the i^{th} and j^{th} synapses, and n is the number of synapses on the neuron. $\overline{u}$ is the average of $K(t)$ derived from 1,000 randomizations of synapse positions on the surface of the dendritic arbor.

A detailed complete description of the experimental procedures can be found in the Supplemental Experimental Procedures accompanying this paper.

SUPPLEMENTAL INFORMATION

Supplemental Information includes Supplemental Experimental Procedures, seven figures, one table, and four movies and can be found with this article online at http://dx.doi.org/10.1016/j.cell.2015.08.033.

AUTHOR CONTRIBUTIONS

Y.M.S., C.M.S., and X.Z. designed the experiments. Y.M.S. and C.M.S. developed the super-resolution reconstruction platform and performed the imaging experiments. H.P.B. wrote software for automated image acquisition and analysis for constructing the STORM images. C.M.S. developed antibody-labeling strategies and performed STORM sample preparation. Y.M.S. developed image alignment, segmentation, and analysis algorithms and performed analysis of STORM datasets. C.M.S., Y.M.S., and X.Z. wrote the paper with input from H.P.B.

ACKNOWLEDGMENTS

We thank Daisy Spear, Mariah Evarts, and Sara Haddad for assistance with animals and Stephen Turney for providing custom confocal imaging equipment. We thank Joshua Sanes, Arjun Krishnaswamy, Melanie Samuel, Jeremy Kay, and the members of the X.Z. lab for discussions during the course of this project. This work was supported in part by Collaborative Innovation Awards of Howard Hughes Medical Institute (HHMI), the National Institute of Mental Health Conte Center Program (P50MH094271), and the Army Research Office MURI program (6019269). X.Z. is a HHMI investigator.

Received: April 18, 2015
Revised: July 22, 2015
Accepted: August 12, 2015
Published: October 1, 2015

REFERENCES

Alivisatos, A.P., Chun, M., Church, G.M., Deisseroth, K., Donoghue, J.P., Greenspan, R.J., McEuen, P.L., Roukes, M.L., Sejnowski, T.J., Weiss, P.S., and Yuste, R. (2013). Neuroscience. The brain activity map. Science *339*, 1284–1285.

Anderson, J.R., Jones, B.W., Watt, C.B., Shaw, M.V., Yang, J.H., Demill, D., Lauritzen, J.S., Lin, Y., Rapp, K.D., Mastronarde, D., et al. (2011). Exploring the retinal connectome. Mol. Vis. *17*, 355–379.

Auferkorte, O.N., Baden, T., Kaushalya, S.K., Zabouri, N., Rudolph, U., Haverkamp, S., and Euler, T. (2012). GABA(A) receptors containing the α2 subunit are critical for direction-selective inhibition in the retina. PLoS ONE *7*, e35109.

Babcock, H., Sigal, Y.M., and Zhuang, X. (2012). A high-density 3D localization algorithm for stochastic optical reconstruction microscopy. Opt. Nanoscopy *1*, 1.

Bargmann, C.I., and Marder, E. (2013). From the connectome to brain function. Nat. Methods *10*, 483–490.

Bleckert, A., Parker, E.D., Kang, Y., Pancaroglu, R., Soto, F., Lewis, R., Craig, A.M., and Wong, R.O. (2013). Spatial relationships between GABAergic and glutamatergic synapses on the dendrites of distinct types of mouse retinal ganglion cells across development. PLoS ONE *8*, e69612.

Brickley, S.G., and Mody, I. (2012). Extrasynaptic GABA(A) receptors: their function in the CNS and implications for disease. Neuron *73*, 23–34.

Briggman, K.L., Helmstaedter, M., and Denk, W. (2011). Wiring specificity in the direction-selectivity circuit of the retina. Nature *471*, 183–188.

Cai, D., Cohen, K.B., Luo, T., Lichtman, J.W., and Sanes, J.R. (2013). Improved tools for the Brainbow toolbox. Nat. Methods *10*, 540–547.

Caldwell, J.H., Daw, N.W., and Wyatt, H.J. (1978). Effects of picrotoxin and strychnine on rabbit retinal ganglion cells: lateral interactions for cells with more complex receptive fields. J. Physiol. *276*, 277–298.

Chklovskii, D.B., Vitaladevuni, S., and Scheffer, L.K. (2010). Semi-automated reconstruction of neural circuits using electron microscopy. Curr. Opin. Neurobiol. *20*, 667–675.

Dani, A., Huang, B., Bergan, J., Dulac, C., and Zhuang, X. (2010). Superresolution imaging of chemical synapses in the brain. Neuron *68*, 843–856.

Dempsey, G.T., Vaughan, J.C., Chen, K.H., Bates, M., and Zhuang, X. (2011). Evaluation of fluorophores for optimal performance in localization-based super-resolution imaging. Nat. Methods *8*, 1027–1036.

Feng, G., Tintrup, H., Kirsch, J., Nichol, M.C., Kuhse, J., Betz, H., and Sanes, J.R. (1998). Dual requirement for gephyrin in glycine receptor clustering and molybdoenzyme activity. Science *282*, 1321–1324.

Feng, G., Mellor, R.H., Bernstein, M., Keller-Peck, C., Nguyen, Q.T., Wallace, M., Nerbonne, J.M., Lichtman, J.W., and Sanes, J.R. (2000). Imaging neuronal subsets in transgenic mice expressing multiple spectral variants of GFP. Neuron *28*, 41–51.

Fischer, F., Kneussel, M., Tintrup, H., Haverkamp, S., Rauen, T., Betz, H., and Wässle, H. (2000). Reduced synaptic clustering of GABA and glycine receptors in the retina of the gephyrin null mutant mouse. J. Comp. Neurol. *427*, 634–648.

Fried, S.I., Münch, T.A., and Werblin, F.S. (2002). Mechanisms and circuitry underlying directional selectivity in the retina. Nature *420*, 411–414.

Gollisch, T., and Meister, M. (2010). Eye smarter than scientists believed: neural computations in circuits of the retina. Neuron *65*, 150–164.

Guizar-Sicairos, M., Thurman, S.T., and Fienup, J.R. (2008). Efficient subpixel image registration algorithms. Opt. Lett. *33*, 156–158.

Hell, S.W. (2007). Far-field optical nanoscopy. Science *316*, 1153–1158.

Helmstaedter, M. (2013). Cellular-resolution connectomics: challenges of dense neural circuit reconstruction. Nat. Methods *10*, 501–507.

Helmstaedter, M., Briggman, K.L., Turaga, S.C., Jain, V., Seung, H.S., and Denk, W. (2013). Connectomic reconstruction of the inner plexiform layer in the mouse retina. Nature *500*, 168–174.

Holden, S.J., Uphoff, S., and Kapanidis, A.N. (2011). DAOSTORM: an algorithm for high- density super-resolution microscopy. Nat. Methods *8*, 279–280.

Huang, B., Wang, W., Bates, M., and Zhuang, X. (2008). Three-dimensional super-resolution imaging by stochastic optical reconstruction microscopy. Science *319*, 810–813.

Huang, B., Babcock, H., and Zhuang, X. (2010). Breaking the diffraction barrier: super-resolution imaging of cells. Cell *143*, 1047–1058.

Huang, F., Hartwich, T.M., Rivera-Molina, F.E., Lin, Y., Duim, W.C., Long, J.J., Uchil, P.D., Myers, J.R., Baird, M.A., Mothes, W., et al. (2013). Video-rate nanoscopy using sCMOS camera-specific single-molecule localization algorithms. Nat. Methods *10*, 653–658.

Ishii, T., and Kaneda, M. (2014). ON-pathway-dominant glycinergic regulation of cholinergic amacrine cells in the mouse retina. J. Physiol. *592*, 4235–4245.

Jain, V., Seung, H.S., and Turaga, S.C. (2010). Machines that learn to segment images: a crucial technology for connectomics. Curr. Opin. Neurobiol. *20*, 653–666.

Jensen, R.J. (1999). Responses of directionally selective retinal ganglion cells to activation of AMPA glutamate receptors. Vis. Neurosci. *16*, 205–219.

Jia, S., Vaughan, J.C., and Zhuang, X. (2014). Isotropic 3D Super-resolution Imaging with a Self-bending Point Spread Function. Nat. Photonics *8*, 302–306.

Kirsch, J., Wolters, I., Triller, A., and Betz, H. (1993). Gephyrin antisense oligonucleotides prevent glycine receptor clustering in spinal neurons. Nature *366*, 745–748.

Kittila, C.A., and Massey, S.C. (1995). Effect of ON pathway blockade on directional selectivity in the rabbit retina. J. Neurophysiol. *73*, 703–712.

Kleinfeld, D., Bharioke, A., Blinder, P., Bock, D.D., Briggman, K.L., Chklovskii, D.B., Denk, W., Helmstaedter, M., Kaufhold, J.P., Lee, W.C., et al. (2011). Large-scale automated histology in the pursuit of connectomes. J. Neurosci. *31*, 16125–16138.

Lichtman, J.W., and Denk, W. (2011). The big and the small: challenges of imaging the brain's circuits. Science *334*, 618–623.

Lim, R., Alvarez, F.J., and Walmsley, B. (1999). Quantal size is correlated with receptor cluster area at glycinergic synapses in the rat brainstem. J. Physiol. *516*, 505–512.

Loulier, K., Barry, R., Mahou, P., Le Franc, Y., Supatto, W., Matho, K.S., Ieng, S., Fouquet, S., Dupin, E., Benosman, R., et al. (2014). Multiplex cell and lineage tracking with combinatorial labels. Neuron *81*, 505–520.

Lowe, D.G. (2004). Distinctive image features from scale-invariant keypoints. Int. J. Comput. Vis. *60*, 91–110.

Majumdar, S., Weiss, J., and Wässle, H. (2009). Glycinergic input of widefield, displaced amacrine cells of the mouse retina. J. Physiol. *587*, 3831–3849.

Massey, S.C., Linn, D.M., Kittila, C.A., and Mirza, W. (1997). Contributions of GABAA receptors and GABAC receptors to acetylcholine release and directional selectivity in the rabbit retina. Vis. Neurosci. *14*, 939–948.

Micheva, K.D., and Smith, S.J. (2007). Array tomography: a new tool for imaging the molecular architecture and ultrastructure of neural circuits. Neuron *55*, 25–36.

Micheva, K.D., Busse, B., Weiler, N.C., O'Rourke, N., and Smith, S.J. (2010). Single-synapse analysis of a diverse synapse population: proteomic imaging methods and markers. Neuron *68*, 639–653.

Miyawaki, A. (2015). Brain clearing for connectomics. Microscopy (Oxf.) *64*, 5–8.

Morgan, J.L., and Lichtman, J.W. (2013). Why not connectomics? Nat. Methods *10*, 494–500.

Nanguneri, S., Flottmann, B., Horstmann, H., Heilemann, M., and Kuner, T. (2012). Three-dimensional, tomographic super-resolution fluorescence imaging of serially sectioned thick samples. PLoS ONE *7*, e38098.

Nusser, Z., Cull-Candy, S., and Farrant, M. (1997). Differences in synaptic GABA(A) receptor number underlie variation in GABA mini amplitude. Neuron *19*, 697–709.

Nusser, Z., Hájos, N., Somogyi, P., and Mody, I. (1998). Increased number of synaptic GABA(A) receptors underlies potentiation at hippocampal inhibitory synapses. Nature *395*, 172–177.

Otsu, N. (1979). A threshold selection method from gray-level histograms. IEEE Trans. Syst. Man Cybern. *9*, 62–66.

Pang, J.J., Gao, F., and Wu, S.M. (2012). Physiological characterization and functional heterogeneity of narrow-field mammalian amacrine cells. J. Physiol. *590*, 223–234.

Punge, A., Rizzoli, S.O., Jahn, R., Wildanger, J.D., Meyer, L., Schönle, A., Kastrup, L., and Hell, S.W. (2008). 3D reconstruction of high-resolution STED microscope images. Microsc. Res. Tech. *71*, 644–650.

Rust, M.J., Bates, M., and Zhuang, X. (2006). Sub-diffraction-limit imaging by stochastic optical reconstruction microscopy (STORM). Nat. Methods *3*, 793–795.

Saalfeld, S., Fetter, R., Cardona, A., and Tomancak, P. (2012). Elastic volume reconstruction from series of ultra-thin microscopy sections. Nat. Methods *9*, 717–720.

Shtengel, G., Galbraith, J.A., Galbraith, C.G., Lippincott-Schwartz, J., Gillette, J.M., Manley, S., Sougrat, R., Waterman, C.M., Kanchanawong, P., Davidson, M.W., et al. (2009). Interferometric fluorescent super-resolution microscopy resolves 3D cellular ultrastructure. Proc. Natl. Acad. Sci. USA *106*, 3125–3130.

Specht, C.G., Izeddin, I., Rodriguez, P.C., El Beheiry, M., Rostaing, P., Darzacq, X., Dahan, M., and Triller, A. (2013). Quantitative nanoscopy of inhibitory synapses: counting gephyrin molecules and receptor binding sites. Neuron *79*, 308–321.

Stafford, B.K., Park, S.J., Wong, K.Y., and Demb, J.B. (2014). Developmental changes in NMDA receptor subunit composition at ON and OFF bipolar cell synapses onto direction-selective retinal ganglion cells. J. Neurosci. *34*, 1942–1948.

Stasheff, S.F., and Masland, R.H. (2002). Functional inhibition in direction-selective retinal ganglion cells: spatiotemporal extent and intralaminar interactions. J. Neurophysiol. *88*, 1026–1039.

Trenholm, S., Johnson, K., Li, X., Smith, R.G., and Awatramani, G.B. (2011). Parallel mechanisms encode direction in the retina. Neuron *71*, 683–694.

Tretter, V., Mukherjee, J., Maric, H.M., Schindelin, H., Sieghart, W., and Moss, S.J. (2012). Gephyrin, the enigmatic organizer at GABAergic synapses. Front. Cell. Neurosci. *6*, 23.

Tyagarajan, S.K., and Fritschy, J.M. (2014). Gephyrin: a master regulator of neuronal function? Nat. Rev. Neurosci. *15*, 141–156.

Vaney, D.I., Sivyer, B., and Taylor, W.R. (2012). Direction selectivity in the retina: symmetry and asymmetry in structure and function. Nat. Rev. Neurosci. *13*, 194–208.

Viswanathan, S., Williams, M.E., Bloss, E.B., Stasevich, T.J., Speer, C.M., Nern, A., Pfeiffer, B.D., Hooks, B.M., Li, W.P., English, B.P., et al. (2015). High-performance probes for light and electron microscopy. Nat. Methods *12*, 568–576.

Völgyi, B., Chheda, S., and Bloomfield, S.A. (2009). Tracer coupling patterns of the ganglion cell subtypes in the mouse retina. J. Comp. Neurol. *512*, 664–687.

Wei, W., Hamby, A.M., Zhou, K., and Feller, M.B. (2011). Development of asymmetric inhibition underlying direction selectivity in the retina. Nature *469*, 402–406.

Werblin, F.S. (2010). Six different roles for crossover inhibition in the retina: correcting the nonlinearities of synaptic transmission. Vis. Neurosci. *27*, 1–8.

Xu, K., Babcock, H.P., and Zhuang, X. (2012). Dual-objective STORM reveals three-dimensional filament organization in the actin cytoskeleton. Nat. Methods *9*, 185–188.

Zhang, C., and McCall, M.A. (2012). Receptor targets of amacrine cells. Vis. Neurosci. *29*, 11–29.

Cell

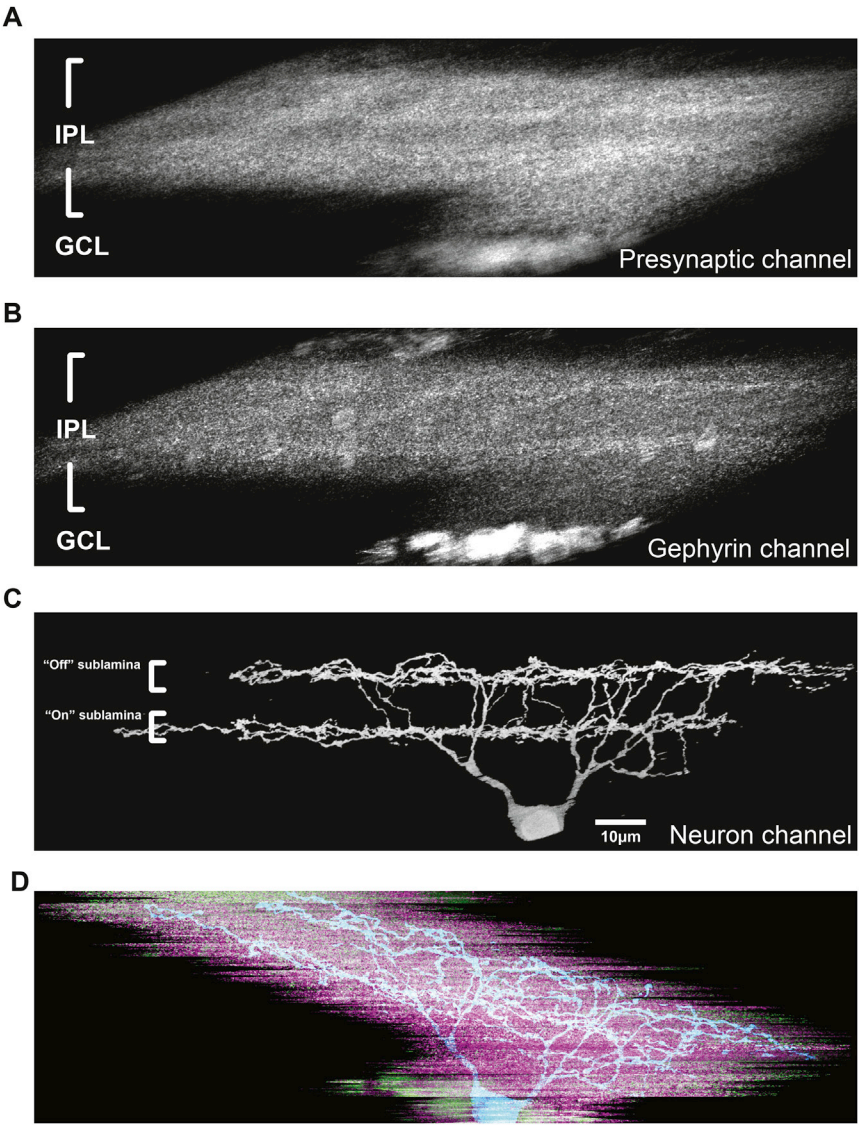

Figure S1. Maximum-Intensity Projection STORM Images of an On-Off DSGC and Surrounding Synapses across the IPL, Related to Figure 1

(A) Presynaptic channel.

(B) Gephyrin channel.

(C) Neuron channel.

Images in (A-C) show a side view that is perpendicular to the sublaminae of the IPL. IPL: inner plexiform layer, GCL: ganglion cell layer.

(D) Merged image of presynaptic (magenta), gephyrin (green), and neuron (blue) channels shown in the viewing angle that allows the serial sections to be seen. This image block was acquired using a combination of single-field imaging (40 μm x 40 μm) near the cell body/proximal dendrites and 2 × 2 mosaic tiling across the remainder of the IPL to capture the dendritic arbor.

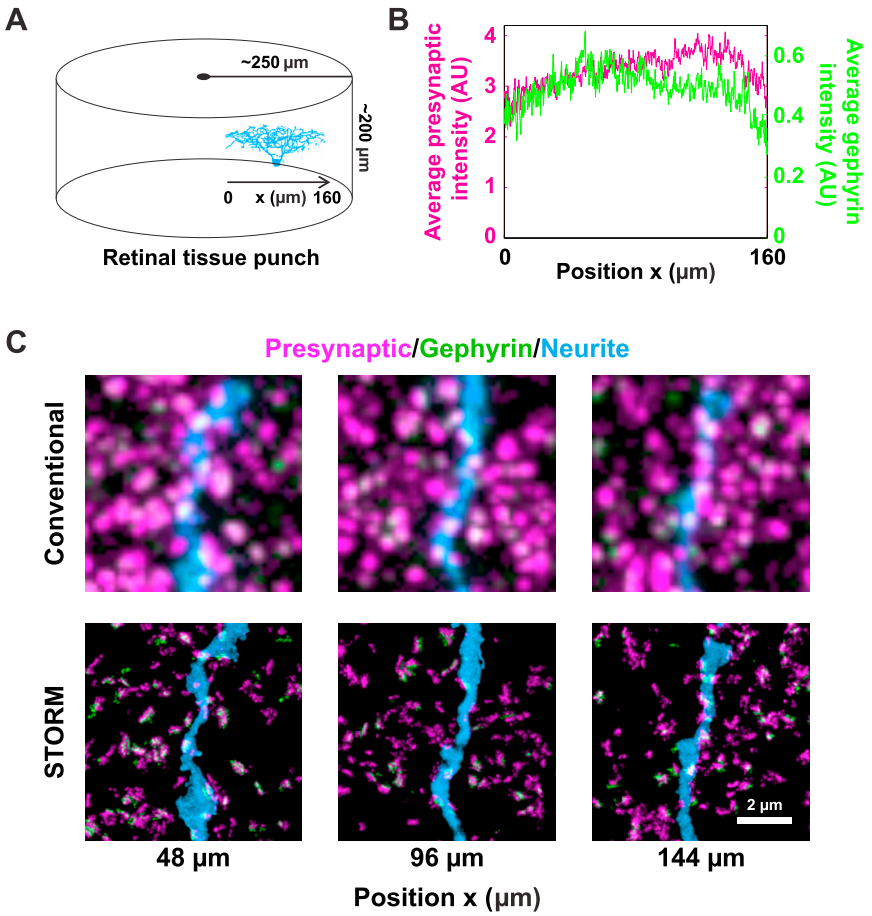

Figure S2. Efficient Antibody Penetration across Retinal Tissue, Related to Figure 1

(A) Schematic of the retinal whole-mount punch containing the On-Off DSGC shown in Figures 1, 2, and 3. The circular punch was ~500 µm in diameter and ~200 µm in thickness. The diameter of the dendritic field of the On-Off DSGC was ~160 µm.

(B) The average signal intensity for presynaptic labeling (magenta) and postsynaptic gephyrin labeling (green) as a function of the *x* position shown in (A).

(C) Representative STORM (lower panels) and corresponding conventional (upper panels) images (500nm Z projections) at three different *x* positions from the center to the periphery of the tissue.

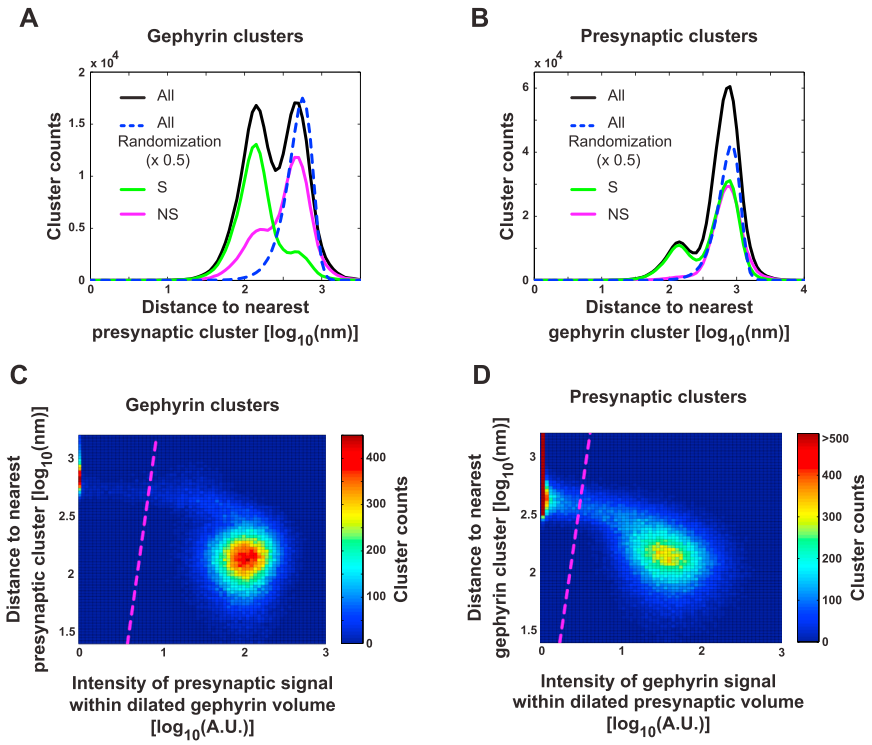

Figure S3. Pairing Analysis of Gephyrin and Presynaptic Clusters, Related to Figure 2

(A) One-dimensional analysis for identifying gephyrin clusters that are paired with presynaptic clusters. Black trace – the distances between all gephyrin clusters and their nearest synaptic clusters in the presynaptic channel follows a bimodal distribution. The smaller-distance peak is consistent with the distance expected for separating presynaptic and postsynaptic scaffolding proteins in synapses, and example pairs of gephyrin and presynaptic clusters drawn from this peak clearly resemble synapses (Figure 2B). The larger-distance peak corresponds to gephyrin clusters with no apposing presynaptic partner, as confirmed by analysis with randomized presynaptic cluster positions. Dashed blue trace – randomizing the positions of the presynaptic clusters collapses the above distribution to a single peak (shown at 1/2 total counts to fit in the same axis scale), the position of which is close to the larger-distance peak before randomization, indicating that this peak corresponds to unpaired gephyrin clusters. Green trace – the distribution of the distances between the putative synaptic (S) gephyrin clusters identified in (Figure 2A) and their nearest presynaptic clusters. Magenta trace – the distribution of the distances between the putative non-synaptic (NS) gephyrin clusters identified in (Figure 2A) and their nearest presynaptic clusters.

(B) One-dimensional analysis for identifying presynaptic clusters that are paired with gephyrin clusters. Similar to (A) but showing the distributions of the distances between various presynaptic clusters and their nearest synaptic gephyrin clusters. Black trace – for all presynaptic clusters. Dashed blue trace – after randomization of the gephyrin cluster positions. Green traces – for putative synaptic (S) clusters in the presynaptic channel. Magenta trace – for putative non-synaptic (NS) clusters in the presynaptic channel.

The distance axes in (A) and (B) are plotted on a log scale.

(C and D) A two-dimensional (2D) analysis for identifying paired gephyrin and presynaptic clusters.

(C) For each synaptic cluster in the gephyrin channel, we determined its distance to the nearest synaptic cluster in the apposing presynaptic channel as well as the mean intensity of presynaptic signal in a dilated volume surrounding this gephyrin cluster. A140nm dilation was used based on the known distance between presynaptic and postsynaptic proteins. The plot is the 2D histogram of the distance and mean intensity distribution constructed from all synaptic clusters identified in the gephyrin channel with the distance and mean intensity plotted on a log scale. The dashed line is the cutoff that splits the distribution into two populations as determined by the OPTICS algorithm followed by linear discriminant analysis.

(D) Similar to (C) except that the analysis is for the synaptic clusters in the presynaptic channel regarding their pairing with gephyrin clusters.

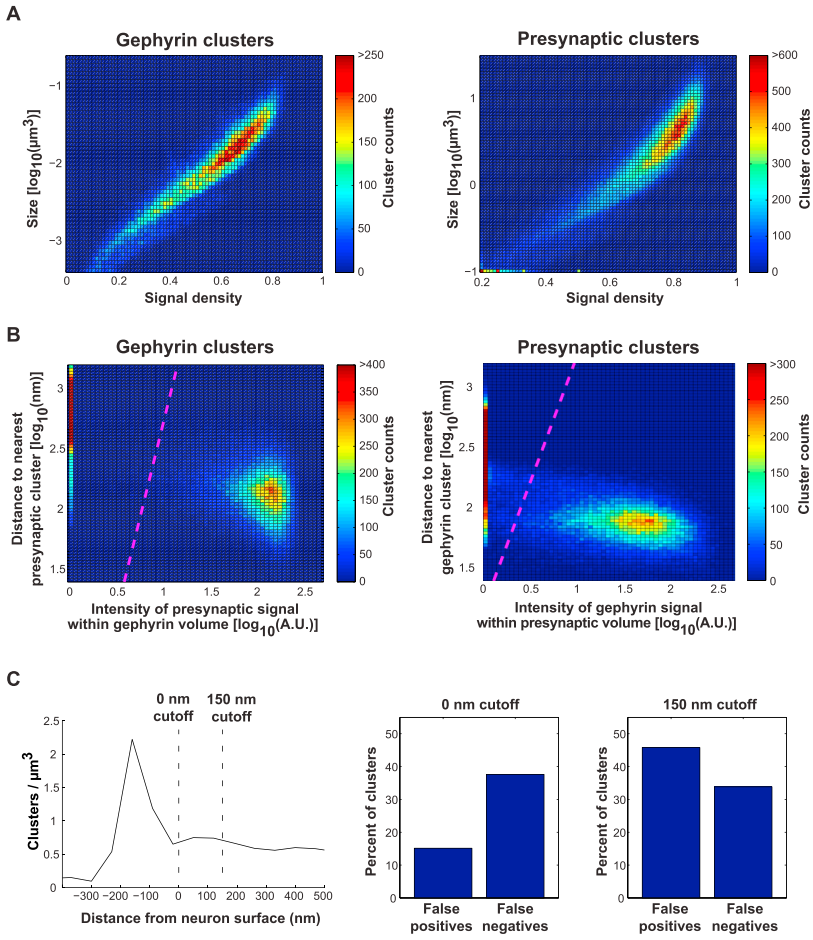

Figure S4. Synapse Identification and Assignment to Neurons Based on Conventional Fluorescence Images, Related to Figure 3

(A) Similar analysis to (Figure 2A) but applied here to the gephyrin and presynaptic clusters identified in the corresponding conventional fluorescence images. As shown in the 2D distribution of the cluster size and signal density for the gephyrin (left) and presynaptic (right) clusters, these clusters cannot be readily separated into distinct populations, unlike the corresponding STORM analysis shown in Figure 2A. This is because the diffraction-limited resolution prevents accurate cluster size and shape determination.

(B) Synapse identification from conventional images based on pairing between presynaptic and gephyrin clusters. Left panel: For each gephyrin cluster, we determined its distance to the nearest cluster in the apposing presynaptic channel as well as the mean intensity of presynaptic signal in the volume occupied by the gephyrin cluster. The plot shows the 2D histogram of the distance and mean intensity values for all gephyrin clusters in the reconstructed volume, with the distance and mean intensity plotted on a log scale. The dashed line is the cutoff that splits the distribution into two populations determined by the OPTICS algorithm followed by linear discriminant analysis. Right panel: Similar to the left panel except that the analysis is for the presynaptic clusters regarding their pairing to gephyrin clusters.

(C) Assignment of synapses (defined as paired gephyrin and presynaptic clusters) to the On-Off DSGC shown in Figure 3E. left: The density of paired gephyrin clusters in conventional images measured as a function of the distance to the neuron surface reveals a peak near the neuron surface, which is substantially broader than the paired gephyrin peak derived from the STORM analysis shown in Figure 3B. From this distribution we set two distance thresholds for assigning synapses to the neuron based on conventional images. The first cutoff is set at the base of this peak (~0 nm), similar to how the cutoff is chosen for the corresponding STORM analysis as shown in Figure 3B. The second cutoff is chosen at 150 nm from the neuron surface reflecting the diffraction-limited resolution. In our imaging system, the diffraction-limited resolution for the Alexa 647 dye is ~300 nm. Therefore, detection of the edge of a structure has an uncertainty that is about half of the resolution, i.e., ~150 nm, which we chose as our second cutoff. To determine the errors in the synapse assignment derived from conventional image analysis, we compared the assignment results to those derived from STORM images. A false positive is defined as a synapse that is assigned to the neuron in the conventional image but not in the STORM image, and a false negative is defined a synapse that is assigned to the neuron in the STORM image but not in the conventional image. Visual inspections confirmed that the STORM assignments in these cases are accurate and the assignments in the conventional images are ambiguous due to blurring by the diffraction-limited resolution (examples are shown in Figure 3D). The percentages of false positives and false negatives for the cutoffs at 0 nm and 150 nm are shown in the middle and right panels, respectively. As expected, the number of false positives increases and that of false negatives decrease as the cutoff is increased. The limited resolution of the conventional image makes it difficult to choose this cutoff value accurately. Similar false positive and false negative errors have been previously observed for synapse analysis based on conventional fluorescence imaging when comparing with EM results (Bleckert et al., 2013; Rah et al., 2013).

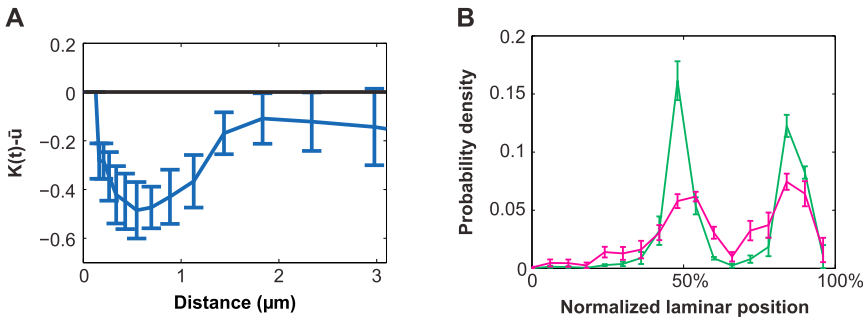

Figure S5. Distribution of Synapses Derived from Six On-Off DSGCs, Related to Figure 4

(A) One-dimensional Ripley's clustering analysis of synapse spacing for the six On-Off DSGCs examined. Ripley's *K* function value is defined in the Experimental Procedures.

(B) The number (green) and density (magenta) of synapses measured as a function of the laminar position on the neuron. 0% represents the beginning of the proximal dendrites just above the cell body and 100% represents the uppermost extent of the dendritic arbor in sublamina S7. Even after normalization for the surface areas of the neurons at different laminar positions, the synapse density (magenta) exhibits two peaks in sublaminae S3 and S7 for all six On-Off DSGCs examined.

The mean values and SEM derived from six neurons are shown.

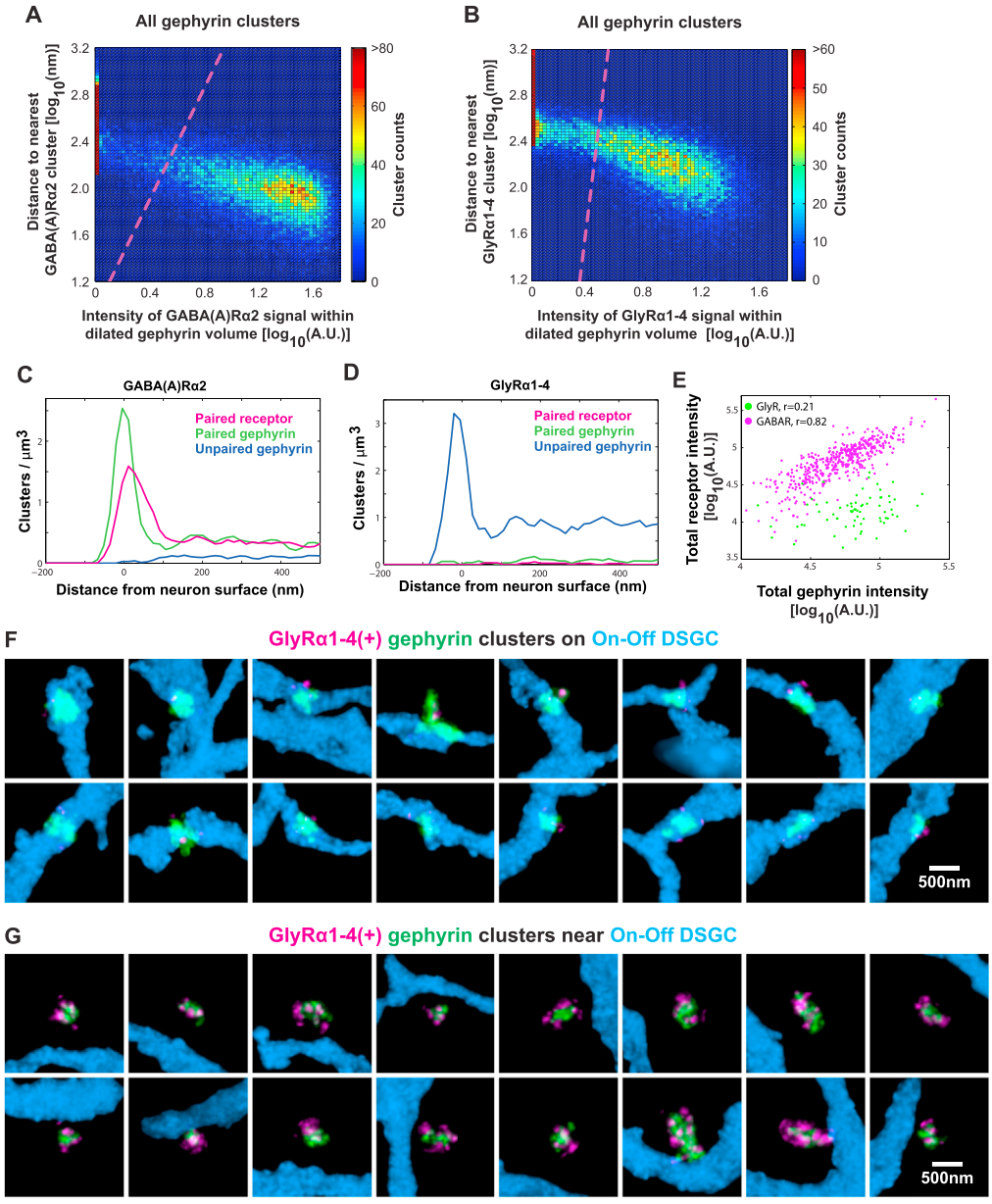

Figure S6. Identification of GABAergic and Glycinergic Synapses on On-Off DSGCs, Related to Figure 5

(A) Pairing analysis between gephyrin and GABA(A)Rα2 clusters. For each synaptic gephyrin cluster, we determined its distance to the nearest GABA(A)Rα2 cluster as well as the mean intensity of the GABA(A)Rα2 signal in a dilated volume surrounding this gephyrin cluster. A 70 nm dilation was used to account for the relatively small distance between receptors and the gephyrin scaffold. The plot is the 2D distribution of the distance and mean intensity constructed from all synaptic gephyrin clusters identified in the image block, with the distance and mean intensity plotted on log scales. Dashed line shows the separation of paired versus unpaired clusters determined by the OPTICS algorithm followed by linear discriminant analysis.

(B) Similar analysis for pairing between gephyrin and GlyRα1-4 clusters.

(C) Quantification of the GABA(A)Rα2-paired gephyrin (green), gephyrin-paired GABA(A)Rα2 receptor (magenta), and unpaired gephyrin (blue) cluster densities as a function of the distance to the surface of an additional On-Off DSGC.

(D) Quantification of the GlyRα1-4-paired gephyrin (green), gephyrin-paired GlyRα1-4 receptor (magenta), and unpaired gephyrin (blue) cluster densities as a function of the distance to the surface of an additional On-Off DSGC.

(E) Correlation plot of the gephyrin intensity and GABA(A)Rα2 (magenta) and correlation plot of the gephyrin intensity and GlyRα1-4 (green) intensity for synapses identified on On-Off DSGCs. The Pearson's correlation coefficient (r) is 0.82 and 0.21, respectively. Total intensities are plotted on a log scale.

(F) Representative examples of GlyRα1-4 positive gephyrin clusters on a On-Off DSGC. GlyRα1-4 is in magenta, gephyrin in green, and the neuron in blue.

(G) Representative GlyRα1-4 positive gephyrin clusters found nearby (< 1 μm from the neuron surface), but not on the On-Off DSGC.

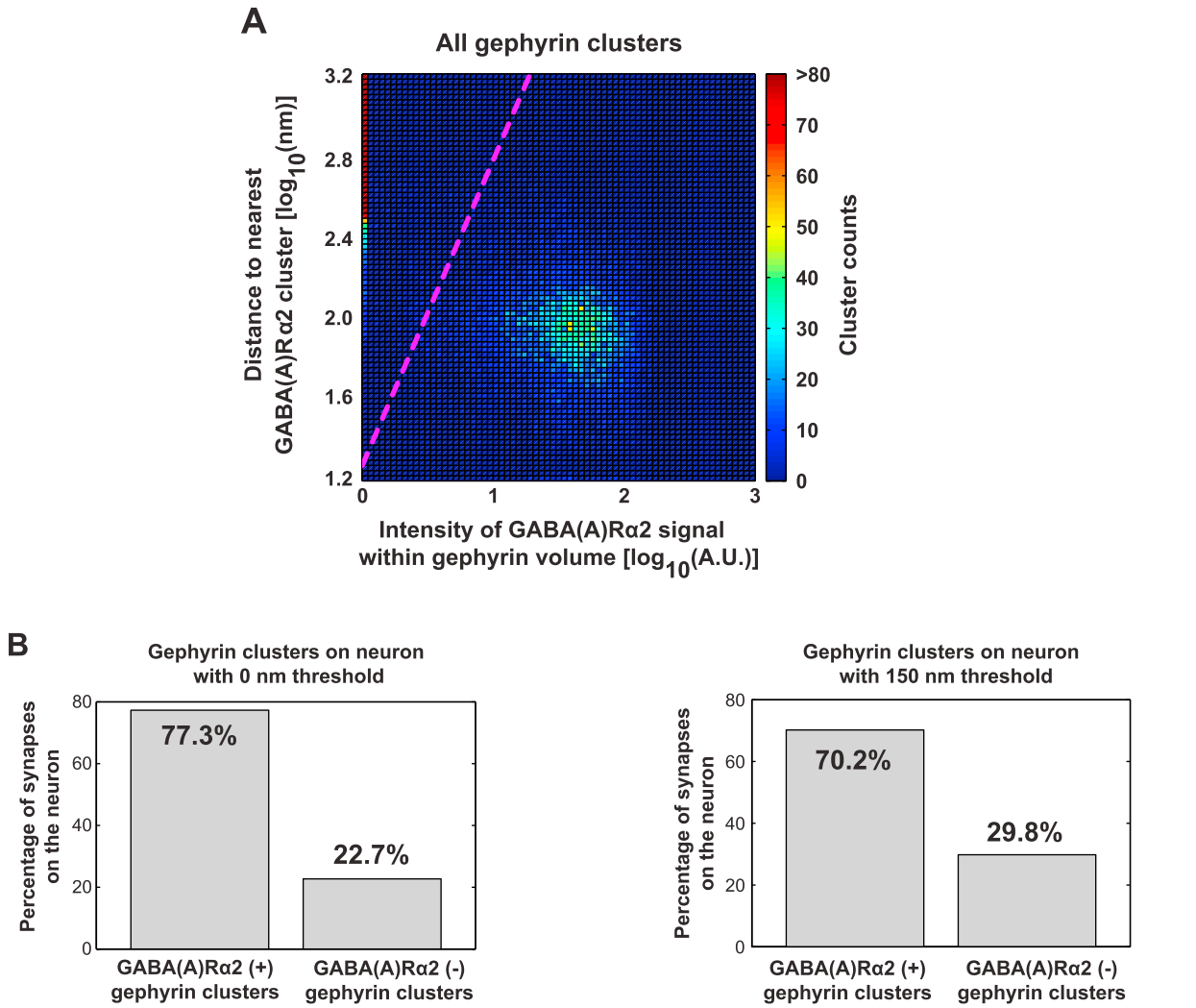

Figure S7. Analysis of GABAergic Synapses on On-Off DSGCs Based on Conventional Images, Related to Figure 5

(A) GABAergic synapse identification from conventional images. For each gephyrin cluster, we determined its distance to the nearest GABA(A)Rα2 cluster as well as the mean intensity of GABA(A)Rα2 signal in a volume occupied by the gephyrin cluster. The plot is the 2D distribution of the distance and mean intensity constructed from all gephyrin clusters in the image block, with the distance and mean intensity plotted on log scales. The dashed line shows a split between GABA(A)Rα2-paired and unpaired populations of gephyrin determined by the OPTICS algorithm followed by linear discriminant analysis.

(B) Quantification of GABA(A)Rα2 positive (+) and GABA(A)Rα2 negative (-) gephyrin clusters on the neuron. Gephyrin clusters are assigned to the neuron based on the 0 nm (left panel) or 150 nm (right panel) cutoffs as described in Figure S4C. In contrast to the STORM analysis which shows that 97% of inhibitory synapses onto On-Off DSGCs are GABA(A)Rα2 positive and only 3% are GABA(A)Rα2 negative, analysis of the corresponding conventional images showed a much larger percentage of GABA(A)Rα2 negative gephyrin clusters. Using the 0 nm cutoff, 23% of the gephyrin clusters on the neuron are GABA(A)Rα2 negative while 30% percent of the gephyrin clusters on the neuron are identified as GABA(A)Rα2 negative using the 150 nm cutoff.

Cell

Supplemental Information

Mapping Synaptic Input Fields of Neurons with Super-Resolution Imaging

Yaron M. Sigal, Colenso M. Speer, Hazen P. Babcock, and Xiaowei Zhuang

Supplemental experimental procedures

Animals

Animal work was performed in accordance with protocols approved by the Institutional Animal Care and Use Committee at Harvard University. Adult transgenic mice (male/female aged ~6-24 weeks) with stochastic expression of GFP or YFP (Tg(Thy-1-EGFP)MJrs/J or Tg(Thy1-YFP)HJrs/J, The Jackson Laboratory, Bar Harbor ME) in retinal ganglion cells (Feng et al., 2000) were used in our experiments. For euthanasia, animals were overdosed (~4ml/kg) with Euthasol (Virbac Animal Health, Fort Worth TX) and perfused with 4% paraformaldehyde diluted in lactated Ringer's solution. In some experiments, eyes were removed following euthanasia without perfusion.

Retinal tissue preparation

Eyes were dissected and whole eye-cups were immersion fixed in 4% paraformaldehyde for 10-60 minutes at room temperature. Retinae were removed and washed in 1X Dulbecco's phosphate buffered saline (DPBS) (Corning, Manassas VA). Both whole-mount and vibratome-sectioned retinae were used for labeling. For whole-mount, retinae were laid flat on nitrocellulose membranes and individual labeled neurons were excised in circular punches (diameter ~500 μm, thickness ~200 μm). For vibratome sectioning, retinae were immersed in 37°C 2-3% agarose, cooled on ice, and sectioned at 50-150 μm thickness in 1X DPBS.

Immunohistochemistry

Retinae were blocked in 10% normal donkey serum (Jackson Immunoresearch, West Grove PA) in 1X DPBS with 0.3% Triton X-100 and 0.02-0.05% sodium azide for 2-3 hours at room temperature. Subsequently, retinae were incubated in primary antibody solutions diluted in blocking buffer overnight for 3-4 nights at 4°C.

We selected primary antibodies first by screening the literature to identify antibodies that had been previously tested in the mouse retina and/or brain to show high-specificity and low background using knockout animals, western blot analysis, and/or control peptide adsorption experiments. After selecting several (typically 2-4) different antibodies for a particular protein target, we tested the performance of each antibody under various conditions of fixation, permeabilization, and incubation time. From these tests, we identified antibodies that provided the highest signal intensity in conventional images and greatest localization density in individual clusters in STORM images, and selected these for additional optimization. Overall, we found excellent correspondence between the fluorescence intensity and signal-to-noise ratio of conventional images and the quality of STORM images during these optimization steps. For gephyrin and GABA receptor, the selected antibodies yielded STORM images that contain large synapse-like clusters (~200-400 nm in diameter) and dense STORM localizations within each cluster (several hundred localizations/cluster). For presynaptic labeling, the selected antibodies yielded STORM images that contained clusters with the above characteristics that were also directly apposed to gephyrin clusters. For glycine receptor antibody labeling we selected antibodies that provided the greatest number of localizations in clusters apposed to postsynaptic gephyrin clusters.

A complete list of all primary antibodies tested in this work is provided in Table S1. The selected antibodies for the volumetric STORM reconstructions are highlighted in the table and listed below: chicken anti-GFP (Life Technologies Cat. #A10262; Grand Island NY; 1:100) was used for neuron labeling, a cocktail containing guinea pig anti-bassoon (Synaptic Systems Cat. #141 004; Goettingen Germany; 1:100), rabbit anti-piccolo (Synaptic Systems Cat. #142 003; 1:100), rabbit anti-Munc 13-1 (Synaptic Systems Cat. #126 103; 1:100) and rabbit anti-ERC 1b/2 (Synaptic Systems Cat. #143 003; 1:100) was used for labeling presynaptic terminals; a mouse monoclonal anti-gephyrin antibody (Synaptic Systems mAb7a Cat. #s 147 011 or 147 021; 1:100) was used for labeling the postsynaptic terminal of inhibitory synapses; a rabbit polyclonal anti-GABA(A)Rα2 antibody (Synaptic Systems Cat. # 224 103; 1:100) was used for labeling GABA(A) receptors containing the α2 subunit; a cocktail of rabbit anti-

GlyRα1 (Synaptic Systems Cat. # 146 003; 1:100), goat anti-GlyRα2 (Santa Cruz Biotechnology Cat. # sc-17279; Dallas TX; 1:50), rabbit anti-GlyRα3 (Millipore Cat. # AB15014; Billerica MA; 1:100) and rabbit anti-GlyRα4 (Millipore Cat. # AB9696; Billerica MA; 1:100) was used for labeling all glycine receptors. The strategy of using antibody cocktails helped increase the labeling coverage of the target structures as well as the localization density within individual target structures.

Following primary antibody incubation, retinae were washed 6 times for 20 minutes each in 2% normal donkey serum in 1x DPBS at room temperature and incubated in secondary antibodies overnight at 4°C for 1-2 nights. The secondary antibodies used were donkey anti-chicken IgY (Jackson Immunoresearch, West Grove PA; 1:100) conjugated to Atto 488 (Sigma, St. Louis MO), donkey anti-mouse IgG (Jackson Immunoresearch; 1:100) conjugated to Alexa Fluor 647 and Alexa Fluor 405 (Life Technologies; Grand Island NY), donkey anti-rabbit IgG (Jackson Immunoresearch; 1:100) conjugated to DyLight 750 (Thermo Fisher Scientific, Rockford IL) and Alexa Fluor 405, donkey anti-goat IgG (Jackson Immunoresearch; 1:100) conjugated to DyLight 750 and Alexa Fluor 405, and donkey anti-guinea pig IgG (Jackson Immunoresearch; 1:100) conjugated to DyLight 750 and Alexa Fluor 405. Retinae were then washed 6 times for 20 minutes each in 1x DPBS at room temperature and incubated overnight in wheat germ agglutinin (WGA) (Vector Labs, Burlingame CA) conjugated to Cy3B (GE Healthcare Bio-Sciences, Piscataway NJ) (3 mg/ml; 1:10 dilution). Finally, retinae were washed 3 times for 20 minutes each in 1x DPBS at room temperature before embedding.

Postfixation, dehydration, and embedding in epoxy resin

Labeled retinae were postfixed for 2 hours at room temperature in 3% paraformaldehyde and 0.1% glutaraldehyde (Electron Microscopy Sciences, Hatfield PA) diluted in 1x DPBS and washed for 20 minutes at room temperature in 1x DPBS. Postfixed retinae were dehydrated in a graded series of ethanol washes (50%/70%/90%/100% two times) for 10-20 minutes each and then incubated in UltraBed Epoxy Resin (Electron Microscopy Sciences, Hatfield PA) solutions of increasing concentration for two hours

each: (75% ethanol/25% resin; 50% ethanol/50% resin; 25% ethanol/75% resin; 100% resin 2 times). Dehydrated resin blocks were then polymerized in UltraBed overnight for 16 hours at 70°C. The graded series of ethanol and resin used here was chosen to minimize overall size changes within the tissue during dehydration and embedding. However, some loss of extracellular space likely still occurred because such loss was observed for similar dehydration and embedding procedures previously used for EM imaging. Regardless, such small volume changes introduced by sample preparation were unlikely to impact our synapse identification and assignment, which only depended on relative distances between synaptic components, and between synaptic proteins and neurons.

Ultrathin sectioning

Ultrathin sections were cut at 70 nm on a Leica UC7 Ultramicrotome (Leica Microsystems; Buffalo Grove IL) using an ultra Jumbo diamond knife (Diatome; Hatfield PA). The section thickness was verified in two independent ways. First, we observed the interference colors of light reflected from the tissue as sections were cut (Peachey, 1958). The ultrathin sections appeared silver, in good agreement with our specified thickness setting of 70nm. We did not observe any sections that appeared either white (<50nm) or gold (>90nm). Second, we employed the "cylindrical diameters method" previously used to measure section thickness in serial-section electron microscopy (Fiala and Harris, 2001). In this approach, we isolated longitudinally sectioned cylindrical regions of labeled dendrites in our STORM reconstructions and measured the diameter of the dendrite within the imaging plane. We then divided this value by the number of serial sections in which the cylinder appeared. From these measurements we estimated our section thickness to be 71.7 ± 1.7 nm (Mean ± S.E.M.; N=80). Chloroform vapor was used to alleviate compression in the sections generated during cutting. Sections were collected on glass coverslips coated with 0.5% gelatin/0.05% chromium potassium sulfate (Sigma; St. Louis MO). Coverslips were dried at 60°C for 25 minutes.

Preparation of coverslips for imaging

Coverslips supporting the tissue sections were immersed in 10% sodium ethoxide solution for 5-20 minutes to etch the embedding resin and expose the dyes to the thiol-containing imaging buffer for optimal photoswitching. The etched tissue sections were then washed, and air-dried. Fluorescent beads were spotted on the coverslips several millimeters from the tissue sections as fiducial markers. We mixed 1μL 715/755 0.1 μm carboxylate-modified FluoSpheres and 8 μL 540/560 0.2 μm carboxylate-modified FluoSpheres (Life Technologies, Grand Island NY) and spotted <1 μL of this solution onto each coverslip to create a high-density bead field. We also diluted this mixture 1:500-750 in 1x DPBS (with $CaCl_2$ and $MgCl_2$) and deposited <1 μL onto each coverslip to create a low-density bead field. Coverslips were washed in H_2O and secured to glass slide flow channels. Flow channels were filled with STORM imaging buffer (10% glucose/17.5 μM glucose oxidase/708 nM catalase/10mM MEA/10 mM NaCl/200mM Tris) and sealed with epoxy.

Imaging setup

Imaging was performed through Olympus UPlanSApo 100x 1.4 NA oil-immersion objectives mounted on Olympus IX71 inverted microscopes with back optics arranged for oblique incident angle illumination. The microscope contained a custom pentaband dichroic and pentanotch filter (Chroma Technology Corp, Bellows Falls VT). A 488 nm Sapphire HP laser (500mW; Coherent, Santa Clara CA), 560 nm fiber laser (2W; MPB Communications Inc., Montreal Quebec), 647 nm fiber laser (1.5W; MPB Communications Inc., Montreal Quebec) and either the 752nm line of a krypton laser (Innova 302C; Coherent, Santa Clara CA) or a 758nm Toptica tapered amplifier BoosTA system (Toptica Photonics; Munich Germany) were used for excitation of the Atto 488, Cy3B, Alexa Fluor 647 and DyLight 750 dyes, respectively. A 405-nm solid-state laser (Cube 405-100C; Coherent, Santa Clara CA) was used for reactivation of dyes. Illumination and image acquisition was controlled by custom software written in Python. Images were acquired on a 256 x 256 pixel region of an Andor iXon3 897 or 897Ultra EMCCD camera through a QV2

quadview image splitter (Photometrics; Tucson AZ). Each pixel was ~158 nm for a total imaging field size of ~40 μm × 40 μm. Axial focus during imaging was maintained in an automated manner as described previously (Dempsey et al., 2011).

Automated image acquisition

Coverslips with tissue section arrays were first imaged at low magnification (using a 4x objective) to find tissue section and fiducial bead field positions. Based on these images, individual regions of interest (ROIs) in tissue sections or bead fields were identified in each section by imaging with a 100x objective in a single color channel at the conventional resolution. ROIs were tagged with stage position coordinates, and an imaging position list was generated by combining the lists of tagged positions of individual sections for the entire coverslip. This position list was then used to generate a master file that controlled laser illumination, camera activation, stage movement, AOTF control, and shutter sequences for automated STORM and conventional imaging.

Each imaging session began with acquiring 36 partially overlapping images of the low-density bead field. For each image, we first excited the 540/560 beads at 488 nm and detected in the Alexa Fluor 647, Cy3B, and Atto 488 channels, followed by excitation of 715/755 beads at 752 nm and detection in the DyLight 750 and Alexa Fluor 647 channels. These low-density bead images were used to generate warping transforms for chromatic aberration correction across different color channels.

Next, each ROI position on the imaging position list of the coverslip was imaged at the conventional resolution in each of the four color channels (DyLight 750, Alexa Fluor 647, Cy3B, and Atto 488) in rapid succession. Because the area covering the neuron of interest on each section was typically larger than a single 40 μm × 40 μm field of view, we applied mosaic imaging and tiled multiple fields of view on each section. In these mosaics, the neighboring image tiles overlapped by 20% on each edge to enable mosaic alignment.

Next, 9 partially overlapping images of the high-density bead field were acquired in each of the four color channels as described above. These dense-bead images were used for two corrections: 1) flat-field correction of conventional images to compensate for non-uniform illumination intensities across the field of view and 2) non-linear lens distortion correction at image field edges. Subsequently, a second round of 36 low-density bead field images were collected as described earlier. This set of bead images was used to estimate the maximum color alignment drift over the course of the conventional image acquisition and thereby confirm the chromatic alignment precision (< 15 nm residual error on average) and long-term system stability.

STORM imaging of individual ROIs were next performed in four color channels. For STORM imaging in the DyLight 750 and Alexa Fluor 647 channels, 405 nm laser excitation was gradually increased to reactivate dyes from the dark to the fluorescent state and maintain an approximately constant number of activation events per imaging frame, and 750 nm and 647 nm lasers were used for imaging the DyLight 750 and Alexa Fluor 647 dyes, respectively. DyLight 750 channel was imaged first for ~4K-4.5K frames at 30 Hz on average for each ROI and the Alexa Fluor 647 channel was subsequently imaged for 6K-7K frames at 60 Hz. Following DyLight 750 and Alexa Fluor 647 imaging of every ROI, Cy3B and Atto 488 channels were imaged with 561 nm and 488 nm excitation sequentially for ~10K frames each at 60 Hz, without any need of the 405 nm activating laser because the 561 nm and 488 nm excitation can spontaneously switch on a small fraction of Cy3B and Atto 488 at steady state for STORM imaging. To ensure that overlapping regions in each montage were not bleached, STORM movies were collected in two passes for each physical section, each consisting of half the total number of frames described above. An optomechanical square mask was also positioned before the back aperture of the microscope to limit illumination to a square field of view. Raw data were written directly to 2TB external hard drives via eSATA link for storage and analysis.

Each individual field of view was acquired with a total imaging time of ~7-8 minutes for all four color channels combined. For an entire neuron as shown in Figures 1-3, the volumetric reconstruction (2.3 x

10^5 μm^3) included ~720 sections and ~4 fields of view per section, and the total imaging time was ~3 weeks. Recent advances in camera technology enable the use of scientific CMOS (sCMOS) cameras with a larger detection area and a faster frame rate for STORM imaging (Huang et al., 2013). Using such a sCMOS camera (ORCA Flash4.0; Hamamatsu Photonics) to replace the EMCCD camera, we recently reduced the imaging time of the same tissue volume to ~3 days.

Chromatic aberration and field-edge distortion correction

Third order polynomial transform maps were generated to correct chromatic aberration between the four color channels. To generate these transformations, thousands of isolated beads were imaged, localized, and mapped over the entire imaging field. Two separate transformations were generated: 1) a transformation for aligning the 750 channel to the 647 channel, using the 715/755 beads and 2) a transformation for aligning the 561 and 488 channels to the 647 channel using the 540/560 beads. The residual error after chromatic aberration correction was <15 nm. In addition to chromatic aberration, we corrected non-linear lens-induced distortions at the edge of each field of view by imaging 3x3 overlapping fields of view of the high-density bead fields on the coverslip and used these images to generate a lens distortion correction transform using the "Distortion Correction" plugin in Fiji (Kaynig et al., 2010) that was then applied to all images. The residual error after the lens distortion correction was <20 nm.

STORM image analysis

All single-field STORM data was analyzed to identify image peaks of individual molecules or partially overlapping molecules and then fit these peaks to generate single-molecule localizations using the previously described DAOSTORM algorithm (Babcock, 2012; Holden et al., 2011). Next, each molecule list was rendered as a 2D image with 15.8 nm pixel size, which is close to both our ~20 nm STORM image resolution and 1/10 of the camera pixel size. For consistency of analysis, the conventional images were up-sampled to 15.8 nm/pixel. Conventional and STORM images were cropped by 5% at the edges

of each field of view to eliminate illumination artifacts caused by the optomechanical mask. Chromatic aberration and lens-induced optical distortions were corrected in all images as described in the above section.

Alignment of multiple image tiles within individual sections

Each STORM image was aligned to the corresponding conventional image using two-dimensional cross-correlation with sub-pixel accuracy (Guizar-Sicairos et al., 2008). When multiple overlapping fields of view were acquired in a section, scale-invariant feature transformation (SIFT) (Lowe, 2004) was used to find points of similarity between overlapping regions in adjacent image tiles in the WGA channel and generate a rigid alignment transform. These transformations were applied to the conventional and STORM images to stitch overlapping image tiles in each section. On average the residual offset in alignment between SIFT points of similarity in two adjacent image tiles was < 40 nm. Since several hundred points of similarity were used to rigidly align adjacent image tiles, we expect the actual error in mosaic stitching to be less than 40 nm.

Conventional and STORM image normalization

The reconstruction of whole neurons required imaging hundreds of sections over many separate coverslips, each of which was imaged for >24 hours on average. Over the course of image acquisition in each coverslip, we noticed a rundown of the imaging buffer that resulted in fewer switching events per dye molecule and hence lower STORM signal intensities near the end of an imaging session compared with the beginning. To correct these intensity variations between serial sections within a dataset, we normalized the intensity histogram constructed from individual pixel values of each section within the IPL by remapping to either the average section histogram of the entire data set or a rolling average histogram that spanned at least two coverslips. STORM and conventional images were normalized across all sections to span the full 8-bit signal range (0-255).

Alignment of serial sections

For serial section alignment, we used either WGA images, or in some cases, a merged image of the WGA and neuron channels. We used the elastic volume reconstruction method described recently (Saalfeld et al., 2012) for registering hundreds of sections. For proper alignment, we proceeded in two steps. First, corresponding SIFT features between adjacent sections were used to determine a rigid linear transformation between sections. This was propagated through all sections in the dataset to achieve a coarse, global, 3D rigid alignment of the data. Second, we applied elastic registration (Saalfeld et al., 2012) that allows non-linear transformation of the images to further improve the alignment accuracy between adjacent sections while minimizing the global deformation of the entire image block. The warping transforms generated in these steps were applied to all conventional fluorescence and STORM channels. On average we found a residual offset of < 80 nm for SIFT points of similarity between adjacent image sections following serial-section elastic registration. Since the individual section thickness is 70 nm, these <80 nm offsets include real shift in the positions of the biological structures between adjacent sections whereas the alignment error should be substantially less than 80 nm.

Segmentation of STORM and conventional fluorescence images

The STORM images were filtered using a mask generated from the conventional images to remove background and signals from occasional debris on the coverslip, and then STORM image intensity normalization was performed according the procedure described in "**Conventional and STORM image normalization**" section. To generate this mask, the signals in the conventional images were thresholded using the lower threshold of a two-level Otsu threshold method (Otsu, 1979). Using the two-level Otsu threshold method with two automatically determined threshold values, we divided the signals in our images into three classes with the lowest-intensity class represents the background, the highest intensity class represents neuronal and synaptic features, and the middle class represents other low intensity signals above background. We used the lower threshold to remove the background signal in the conventional

images and generate a filter mask, which was then applied to the STORM images to remove the background and debris signals.

For segmentation of the neuronal channel, we determined the largest connected component of neuronal signal within the STORM dataset. We also included isolated neuronal signal separated from the largest connected component by less than 2μm. Since the labeled neurons in YFP-H and GFP-M mice were sparse and non-overlapping, these unconnected neuron signals necessarily all arose from the same neuron. To identify the surface of the neuron, we smoothed the neuron signal with a Gaussian kernel with σ = 47 nm and then binarized the neuron signal using the lower threshold of the two-level Otsu threshold method. For some analyses, a linear skeleton of the neuron was also calculated using a 3D medial surface thinning algorithm (Kerschnitzki et al., 2013; Lee, 1994).

To identify fluorescent clusters in the gephyrin, presynaptic or receptor channels in the STORM images, we first applied a 79 nm Gaussian convolution to the signal in the XY plane and an isometric Gaussian convolution (~1 voxel) in Z. We then used the lower threshold of the two-level Otsu threshold method to binarize the image and identify connected components in three dimensions. Additional separation of over-connected clusters was performed using a watershed transform that is based on the distance to and intensity gradient near local intensity maxima in the image (Gonzalez et al., 2003; Soille, 2010).

Processing of conventional images was carried out in the same manner as for the STORM data, except that we binarized the conventional images based on the higher threshold of a two level Otsu threshold.

Distance measurements to the surface of the neuron

The distance between the synaptic clusters and the surface of the neuron was calculated as the intensity-weighted mean distance between the signal-positive voxels in the synaptic clusters and the nearest voxels on the surface of the neuron. Any distance inside the neuron signal was assigned a negative value for the distance relative to the neuron surface.

Two-dimensional (2D) analysis to separate different populations of gephyrin and presynaptic clusters

To determine whether a given cluster was synaptic, two parameters were considered for each cluster in the gephyrin and presynaptic channels. First, the volume of the cluster was calculated from the connected component within the segmented image. Second, the signal density was measured as the fraction of volume of the connected component that was occupied by signal-positive voxels in the raw data. For STORM images, plotting the distribution of these two parameters constructed from all clusters in the data set as a 2D histogram clearly showed two peaks. To separate the two populations, we fit the cluster volume distribution at each fixed signal density value in the 2D histogram to two Gaussian functions and chose a cutoff point that was 95% of the Gaussian fit area of the smaller-volume cluster population. These cutoff points were fit to a 3rd order polynomial to separate the two populations.

2D analysis for identifying paired synaptic clusters

In this analysis, we determined whether clusters in the gephyrin channel were paired with clusters in the presynaptic channel in the STORM images using two parameters. The first parameter was the distance from the centroid of the gephyrin cluster to the nearest cluster in the apposing presynaptic channel. The second parameter was the mean intensity of presynaptic signal within a dilated region harboring the gephyrin cluster. A 140nm dilation was used for the STORM analysis based on the distance between presynaptic and postsynaptic proteins. The distribution of the distance and intensity parameters constructed from all gephyrin clusters in the image block was then plotted as a 2D histogram. We used the OPTICS algorithm, a variant of DBSCAN capable of discriminating populations with different object densities (Ankerst, 1999), to identify paired and unpaired populations. We applied linear discriminant analysis to best separate the two populations identified by the OPTICS algorithm. This analysis was repeated for pairing of presynaptic clusters with gephyrin. We also used the same approach to evaluate whether gephyrin clusters were paired with receptor clusters, except that a 70 nm dilation to account for

the shorter distance between receptors and the gephyrin scaffold. We applied the same analyses to the conventional fluorescence images, but as the diffraction-limited resolution represented a volume larger than the true object size, no further dilation was applied.

Ripley's K function

The Ripley's *K* function is calculated as $K(t) = \lambda^{-1} \sum_{i \neq j} I(d_{ij} < t)/n$, where t is the distance along neurites, λ is the average density of synapses on the neuron skeleton, I is the indicator function, d_{ij} is the distance between the i^{th} and j^{th} synapses, and n is the number of synapses on the neuron. $\bar{u}$ is the average of $K(t)$ derived from 1000 randomizations of synapse positions on the surface of the dendritic arbor.

Analysis software

All analyses were performed using custom image processing routines written in Python, Matlab, and Jython along with existing image processing programs either on a desktop computer (24 CPU 2.66GHz processor with 24GB RAM) or on the Odyssey cluster supported by the FAS Division of Science, Research Computing Group at Harvard University. The analysis codes developed in this work are available upon request.

Table S1: Antibodies used for labeling neurons and inhibitory synapses in the retina

Presynaptic

Target protein	Species	Clone	Subtype	Catalogue #	Supplier
Bassoon	Rabbit	Polyclonal		ab76065	Abcam
Bassoon	Mouse	SAP7F407	IgG2a	VAM-PS003	Enzo
Bassoon	Rabbit	Polyclonal		141 002	Synaptic Systems
Bassoon	Guinea Pig	Polyclonal		141 004	Synaptic Systems
ERC 1	Mouse	ELKS-30	IgG2a	ab50312	Abcam
ERC 1b/2	Rabbit	Polyclonal		143 003	Synaptic Systems
Munc 13	Rabbit	Polyclonal		ab101740	Abcam
Munc 13-1	Rabbit	Polyclonal		126 102	Synaptic Systems
Munc 13-1	Rabbit	Polyclonal		126 103	Synaptic Systems
Piccolo	Rabbit	Polyclonal		ab20664	Abcam
Piccolo	Goat	Polyclonal		sc-18569	Santa Cruz Biotechnology
Piccolo	Rabbit	Polyclonal		142 002	Synaptic Systems
Piccolo	Rabbit	Polyclonal		142 003	Synaptic Systems

Postsynaptic

Target protein	Species	Clone	Subtype	Catalogue #	Supplier
Gephyrin	Chicken	Polyclonal		ab136343	Abcam
Gephyrin	Goat	Polyclonal		sc-32561	Santa Cruz Biotechnology
Gephyrin	Goat	Polyclonal		sc-32562	Santa Cruz Biotechnology
Gephyrin	Goat	Polyclonal		sc-6411	Santa Cruz Biotechnology
Gephyrin	Rabbit	Polyclonal		147 002	Synaptic Systems
Gephyrin	Rabbit	Polyclonal		147 003	Synaptic Systems
Gephyrin	Mouse	mAb7a	IgG1	147 011	Synaptic Systems
Gephyrin	Mouse	mAb7a	IgG1	147 021	Synaptic Systems
GABA(A)Ra2	Mouse	N399/19	IgG1	73-384	NeuroMab
GABA(A)Ra2	Rabbit	Polyclonal		224 103	Synaptic Systems
GlyRa1	Mouse	mAb4a	IgG1	146 011	Synaptic Systems
GlyRa1	Rabbit	Polyclonal		146 003	Synaptic Systems
GlyRa2	Goat	Polyclonal		sc-17279	Santa Cruz Biotechnology
GlyRa3	Goat	Polyclonal		sc-17282	Santa Cruz Biotechnology
GlyRa3	Rabbit	Polyclonal		AB15014	Millipore
GlyRa4	Rabbit	Polyclonal		AB9696	Millipore
GlyRb	Mouse	299E7		146 211	Synaptic Systems

Neuron

Target protein	Species	Clone	Subtype	Catalogue #	Supplier
GFP	Chicken	Polyclonal		ab13970	Abcam
GFP	Chicken	Polyclonal		A10262	Invitrogen
GFP	Rabbit	Polyclonal		A-11122	Invitrogen
GFP	Rabbit	Polyclonal		JM-3999-100	MBL
GFP	Rabbit	Polyclonal		AB3080	Millipore

Table S1: Antibodies used for labeling neurons and inhibitory synapses in the retina

Table S1 shows all antibodies tested for labeling various synaptic proteins, as well as GFP/YFP-labeled neurons in the retina. The antibodies selected for volumetric STORM reconstructions are highlighted in blue.

Supplemental References

Ankerst, M., Breunig, M.M., Kriegel, H.P., Sander, J. (1999). OPTICS: Ordering points to identify the clustering structure. Proceedings of the ACM SIGMOD International Conference on Management of Data *28*, 49-60.
Fiala, J.C., and Harris, K.M. (2001). Cylindrical diameters method for calibrating section thickness in serial electron microscopy. Journal of microscopy *202*, 468-472.
Gonzalez, R.C., Woods, R.E., and Eddins, S.L. (2003). Digital Image Processing Using MATLAB (Prentice-Hall, Inc.).
Kaynig, V., Fischer, B., Muller, E., and Buhmann, J.M. (2010). Fully automatic stitching and distortion correction of transmission electron microscope images. Journal of structural biology *171*, 163-173.
Kerschnitzki, M., Kollmannsberger, P., Burghammer, M., Duda, G.N., Weinkamer, R., Wagermaier, W., and Fratzl, P. (2013). Architecture of the osteocyte network correlates with bone material quality. Journal of bone and mineral research : the official journal of the American Society for Bone and Mineral Research *28*, 1837-1845.
Lee, T.C., Kayshap, R.L., Chu C.N. (1994). Building skeleton models via 3-D medial surgace axis thinning algorithms. Computer Vision, Graphics, and Image Processing *56*, 462-478.
Peachey, L.D. (1958). Thin sections. I. A study of section thickness and physical distortion produced during microtomy. The Journal of biophysical and biochemical cytology *4*, 233-242.
Rah, J.C., Bas, E., Colonell, J., Mishchenko, Y., Karsh, B., Fetter, R.D., Myers, E.W., Chklovskii, D.B., Svoboda, K., Harris, T.D*., et al.* (2013). Thalamocortical input onto layer 5 pyramidal neurons measured using quantitative large-scale array tomography. Frontiers in neural circuits *7*, 177.
Soille, P. (2010). Morphological Image Analysis: Principles and Applications (Springer Berlin Heidelberg).